Interpretation of Radarsat SAR scenes of Sagwon Alaska, to establish temporal, spatial and physical active layer behavior.

By

Joseph Thomas Lovick

RECOMMENDED :

Advisory committee chair

Chair, Department of Geology and Geophysics

APPROVED:

Dean, College of Science, Engineering and Mathematics

Dean of the Graduate School

6-9-03

Date.

Interpretation of Radarsat SAR scenes of Sagwon Alaska, to establish temporal, spatial and physical active layer behavior.

A THESIS

Presented to the Faculty of the University of Alaska Fairbanks

In Partial Fulfillment of the Requirements for the Degree of

Master of Science

By

Joseph Thomas Lovick, BSc.

Fairbanks, Alaska

May 2003

Abstract

Radarsat SAR images of the Kuparuk Basin in North Alaska can be used to describe the timing and characteristics of the seasonal freeze-thaw cycle and the spatial distribution of two types of Arctic Tundra. The freezing of the ground surface; decreases backscatter brightness by 3dB allowing the date of freeze-up and thaw to be established. Using Empirical Orthogonal Functions on amplitude images allows the subtle change in the brightness (during winter) of different tundra types to be enhanced, which provides a technique for discriminating between areas of Moist Acidic Tundra and Moist Non-acidic Tundra. The sand to clay ratio affects the backscatter properties of frozen soil and is inferred to cause this brightness difference.

Coherence images show the dynamic nature of Arctic tundra, and low coherence limits the applicability of interferometric techniques to describe active layer heave, however, preliminary results show promise in the application of a differential interferometric technique.

Table of Contents.

List of Figures.

List of Tables

List of Appendices

Acknowledgements

The Author would like to thank Shusun Li for providing the opportunity to carry out this work, my graduate committee for help in revising this thesis; also Kevin Engle and Lynn McNutt for their support, and the graduate students of the 4th Floor of the GI, for their unerring enthusiasm and support.

In addition many, many thanks are to be extended to Steve and Ann, Bob and Winnie for providing me with the opportunity of coming to Alaska, and Yiming for keeping me sane.

Introduction

The further development of a remote sensing technique to study the properties of Arctic tundra would allow detailed information to be recorded on the length of time temperatures are bellow freezing and also map the variations in tundra type. This information would be useful in refining regional climate models, biological productivity estimates and in studies of the behaviour of the Active layer. Ideally this technique would not suffer from the limitations of cloud cover and would provide information though some degree of snow cover.

The principle tool of this investigation is imagery from the C-band HH active microwave sensor on the Canadian remote sensing satellite Radarsat. Radarsat has eight different imaging modes, from which we chose to use the Standard beam, with a nominal ground resolution of $\approx$ 20m x 20m after multi-looking 4 times [Raney 1998]. Within Standard Beam there are seven beam modes (1-7) corresponding to different look angles. we use beams 5 through 7, giving a spread of look angles from 36.5° to 49.4° As a result, radar foreshortening varies between 50.0% to 23.4% [Lewis and Henderson 1998]. This degree of foreshortening is less than that of the other beams which have smaller look angles.

In addition to the radar images, a small number of Moderate Resolution Imaging Spectroradiometer (MODIS) and the Advanced Very High Resolution Radiometer (AVHRR) images were examined to confirm the dates of freeze-up and thaw, and to establish the surface tundra type, as well as the degree, and distribution of snow cover.

Using a technique based on Empirical Orthogonal functions [Eslinger et al. 1989], the radar scene time series is analysed within each beam mode and, as a result of this analysis, the visibility of the boundary between moist acidic tundra and non-acidic tundra is enhanced.

A time series of calibrated radar backscatter images show the effects of freeze up of the surface soil layer and the subsequent spring thawing on radar backscatter.

With a pair of radar scenes of the same beam mode from repeat orbits, it is possible to apply an interferometric synthetic aperture radar (INSAR) technique to establish a detailed estimate of the topography within the scene [Zebker and Goldstein 1986]. The quality of the digital elevation model derived is dependent on a number of factors including instrument performance, orbit parameters, data processing effects, level of coherence between the scenes, and atmospheric conditions. [Zebker et al. 1994].

The processing of radar scenes from January 2000 to December 2001 has resulted in a small number of image pairs that are suitable for use in this study. From these some general trends are evident. Coherence is degraded strongly in scenes obtained between January and May in both years, making derived products very poor in nature. The level and distribution of coherence within the scenes is indicative of certain terrain types and properties, which can be used to estimate the distribution of active layer heave within the study area.

From these scenes a further set of imagery was produced using a technique called Differential Interferometric Synthetic Aperture Radar (SAR), in which four Synthetic Aperture Radar (DINSAR) scenes are used to establish the amount of surface elevation change between two SAR scene pairs. The accuracy of this method is of the same order or finer than the illuminating wave length, $\approx$ 5.7 centimetres with C-band Radar [Li and Wang 1999]. This technique is the primary tool in determining the amount and distribution of active layer heave over a large geographic area.

This work is centred on a region in the Kuparuk river basin centred upon Sagwon, Alaska (76.95N 148.7W) in the North Slope of Alaska. The North Slope of Alaska is a tundra-dominated environment that has come under increasing

study in recent years. This area is extensively underlain with permafrost and is important as a carbon-sink and methane source. Microbial life and vegetation is reliant on the top layer of soil, known as the Active Layer, that experiences a yearly freeze-thaw cycle.

Many previous studies of arctic tundra have classified the plant species and have focused on a number of study sites within the Kuparuk basin, (Figure 1.1). This area has the advantage of falling along side the Dalton Highway, allowing easy access for field work.

Tundra within the Alaskan North Slope can be broadly categorized into two units, differentiated according to soil chemistry. These are known as Moist Acidic Tundra (MAT) pH > 6.5 and Moist Non acidic Tundra (MNT) pH < 5.5. Vegetation differences between these two regions have a strong impact on land-atmosphere exchanges of CO_2, methane, and trace gasses. The MAT has a significantly high biomass and an active layer of shallower depth. The MNT has a more mineral rich soil, less vegetation, and, as a result, significantly lower methane emission and CO_2 uptake. The Regional distribution of MNT and MAT is shown in Figure 1.2 [Walker et al. 1998].

Field data in the form of ground measurements of temperature and soil heave were collected by Vladimir Romanovsky. These are used to ground-truth our remote sensing imagery. Weather data from permanent stations was also integrated, to provide a regional view of temperature variation.

This document is a thesis submitted for the Master of Science degree, awarded by the University of Alaska Fairbanks, addressing (1) the timing and character of seasonal ground freezing; (2) the spatial distribution of two types of arctic tundra; and (3) the distribution active layer heave.

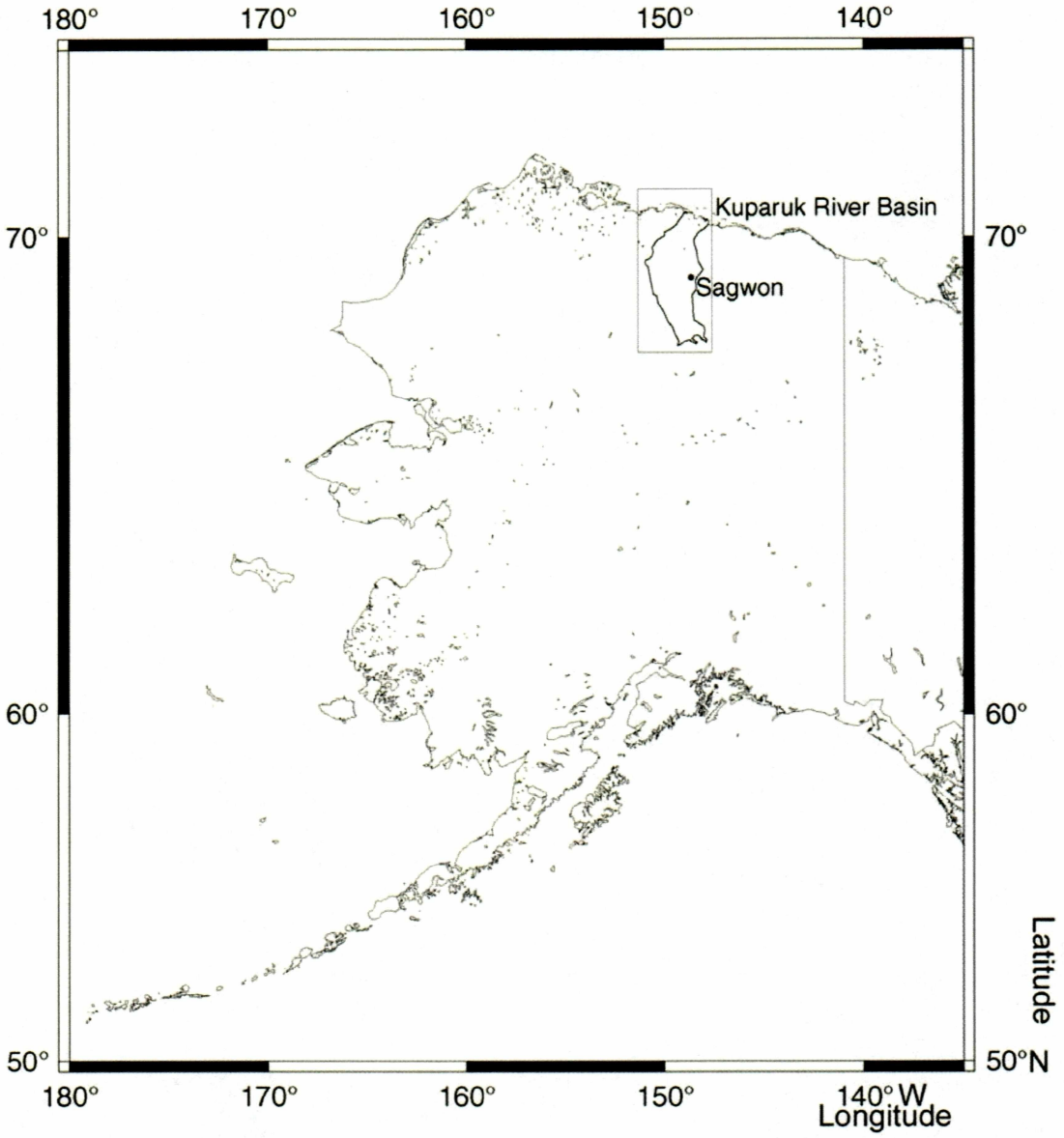

Figure 1.1, The State of Alaska and the Kuparuk River Basin.

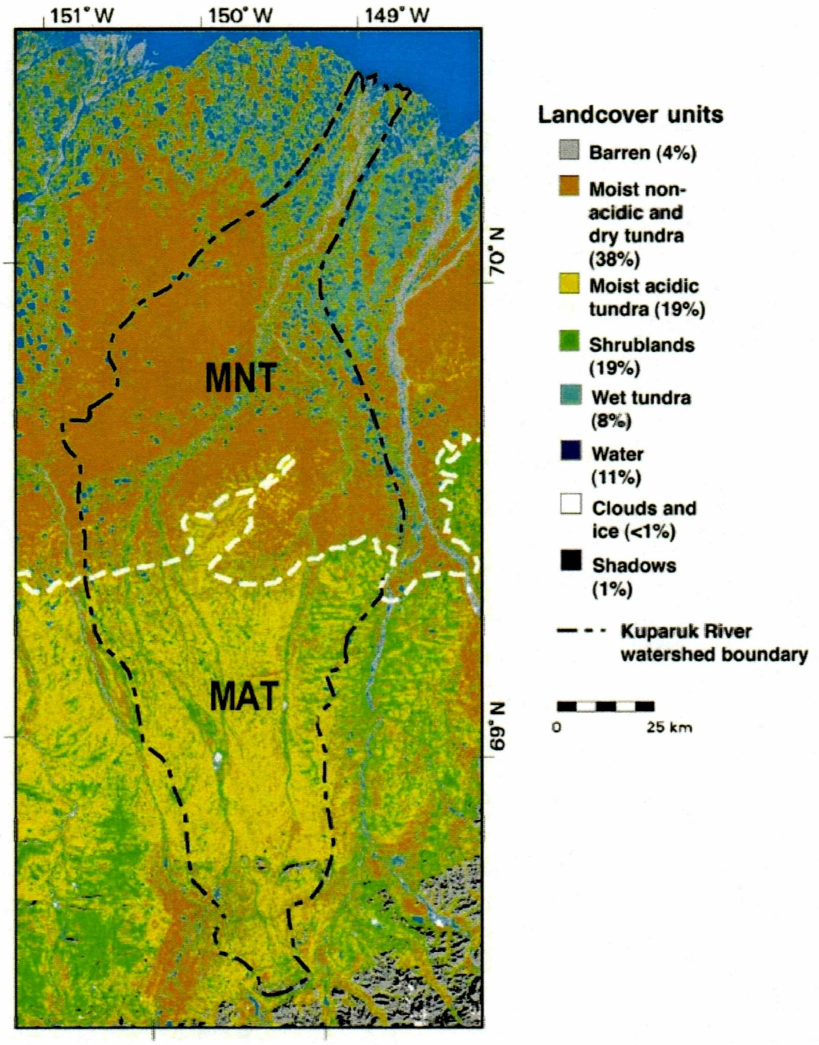

Figure 1.2, The Kuparuk basin with the boundary between MNT and MAT shown as a white dashed line, (from Walker et al. 1998.)

Background

A process for the detailed mapping of permafrost and active layer distribution on a regional scale has long been in demand. Such information is useful in a number of disciplines from global climate modeling to engineering and natural hazard mitigation. The need for reliable and detailed information is urgent because the Arctic is an important part of the global climate system with strong influence and feedback on a large number of earth systems.

The arctic plays a crucial role in global climate. The effects of global warming occur first and with greatest expression in the Arctic. It is also in the Artic where the degree of biocomplexity may allow understanding of the complex systems of biofeedback that dominate the natural earth.

Permafrost is a term used to describe any area of ground that remains at a temperature bellow freezing for a nominal period of greater than two years. The Active Layer is a soil layer that overlies permafrost, which freezes and thaws in the seasonal cycle.

Permafrost and the active layer play a crucial role in the Arctic system, and the role of land hydrological cycles hinges explicitly on permafrost-rich ground, as almost all biologic and hydrological processes occur in the active layer [McMichael et al. 1997].

The thickness of the active layer depends upon annual temperature fluctuations. For instance, an increase in active layer thickness can indicate the shrinkage of the underlying permafrost body. Long-term shrinkage of the permafrost body is an indicator of climate warming.

Previous mappings of permafrost distribution use a combination of techniques [Lewkowicz et al. 1999, Peddle et al. 1993]. However none are fool proof and the addition of a SAR based technique can only increase the options available for large and regional scale classification of land surfaces. Previous

classification studies can be broadly classified into three groups. Those that use remote sensing and image data to isolate regions of particular tundra / permafrost type; those that use a modeled approach to infer the active layer / permafrost / tundra type from the thermal flux, ground inclination, and other spot-measured / modeled factors to then infer the environment at larger scales; and those that use a hybrid approach of combining remote sensing and model based results.

Remote sensing studies have primarily taken two routes: 1) Using vegetation species as indicators of environment and classifying different types of tundra that are indicative of different soil environments [Muller et al. 1999] and 2) using surface landforms to indicate the underlying permafrost bodies [Lewkowicz and Dugauy 1999].

From the alternative model based approaches there seems to be a broadly similar accuracy in describing the active layer / permafrost spatial distribution at about 80% accuracy. Thermal models of North Slope permafrost régime provide reasonable success in larger scale prediction and mapping of permafrost. For example Hinzman et al. [1998] are able to explain $\approx$ 80% of the spatial variance of active layer thickness. This model worked on a 1 km grid using weather data and incoming radiation flux. An example hybrid study of permafrost depth classification from SPOT panchromatic imagery [Peddle and Franklin 1993] uses a complex "evidential-reasoning"[1] based system. Using the spectral properties of the surface layer, the distribution and type of vegetation, surficial geology, water content, and a Digital Elevation Model (DEM) derived from aerial photographs they were able to classify a test region into four categories with a $\approx$ 79% spatial classification accuracy at the 400 ground sample points.

---

[1] Evidential Reasoning in this context represents a classification system that integrates a non-image dataset into a component classification system, with simple parameters guiding the software interpretation of that data.

SAR Backscatter images and the Arctic tundra environment

The ability to isolate the freeze and thaw processes in SAR backscatter imagery would serve a number of uses. The length of the growing season of Arctic tundra depends on the length of the period of sub-zero temperatures. Knowing the length of the growing season allows accurate analysis of productivity, biogeochemical fluxes, and hydrological fluxes [Rignot et al. 1994].

Traditional techniques used to constrain the frozen period have focused on optical imagery (typically AVHRR/MODIS derived products) and used the thermal infrared signal to identify the ground surface temperature [Wan and Dozier 1989]. Cloud cover limits the coverage of the ground surface that can be obtained from optical imaging. Because clouds can be dense during the transitional periods May/June and September, optical imaging is less effective than radar imaging in the Arctic.

One of the most basic questions to be answered is how the backscatter signal of the Artic tundra is affected by the freezing of the surface soil layer. This behaviour has been studied by a number of researchers, principally Ulaby et al. [1998], Wegmüller [1989] and Mironov et al. [2000]. Their works identify a number of factors that influence the characteristics of radar backscatter from soil at temperatures below and above freezing. The radar backscatter characteristics of any medium in the microwave spectra are controlled by the medium's dielectric constant and the surface roughness. A higher dielectric constant implies a greater radar reflectivity and in turn a greater prospective signal return.

The dielectric constant of soils depends on a number of factors including the texture (grain size make up), the temperature, moisture content, and salinity. In backscatter analysis, each of these factors is modulated by the angle of incidence of the microwave beam and the frequency of that beam. For temperatures above freezing the dielectric constants of soils tend to scale with

increasing water content (Figure 3.1.a). The effect of texture is less pronounced than that of water content but still has a strong input: It is approximately proportional to the sand content and inversely related to the clay content (Figure 3.1.a) [Hallikainen et al. 1985].

The Arctic tundra environment has a varying degree of surface vegetation that will affect the backscatter signal. Leaf index, canopy height, stem thickness, total biomass, and plant water content are the dominating vegetation factors [Brisco and Brown 1998]. Coupled with these factors, snow has a strong and complex backscatter effect [Koskinen et al. 2000].

To asses the relative importance of the different factors that affect radar backscatter, a number of SAR time-series were examined of the same source region. Primary work to isolate the images within which the temperature of the ground is at or bellow freezing was conducted across all the Radarsat beam modes and scenes.

Table 3.1 shows the timing of the freeze-up event at several field sites in the North Slope, and also a regional mean temperature derived from national weather service data from the following stations: Deadhorse, Franklin Bluffs, Galbraith Lake, Happy Valley, Kuparuk Airport, Nuiqsut, Oliktok, Umiat and Prudhoe Bay. By correlating these dates with the occurrence of SAR images within our archive we can establish the change in backscatter coefficient (dB) resulting from freezing of the soil surface which occurs over a period of approximately one week each year. Figure 3.2 shows the date occurrence of our SAR scenes in relation to regional temperatures.

Two types of ASF SAR product were used in the study, Standard Beam Complex images and Lowres amplitude images. Each of the Lowres Amplitude scenes was calibrated in the archive and also georeferenced, as well as corrected for topography. A small study region (60km by 60km) that is present in the majority of images was chosen to be indicative of the scene as a whole and its

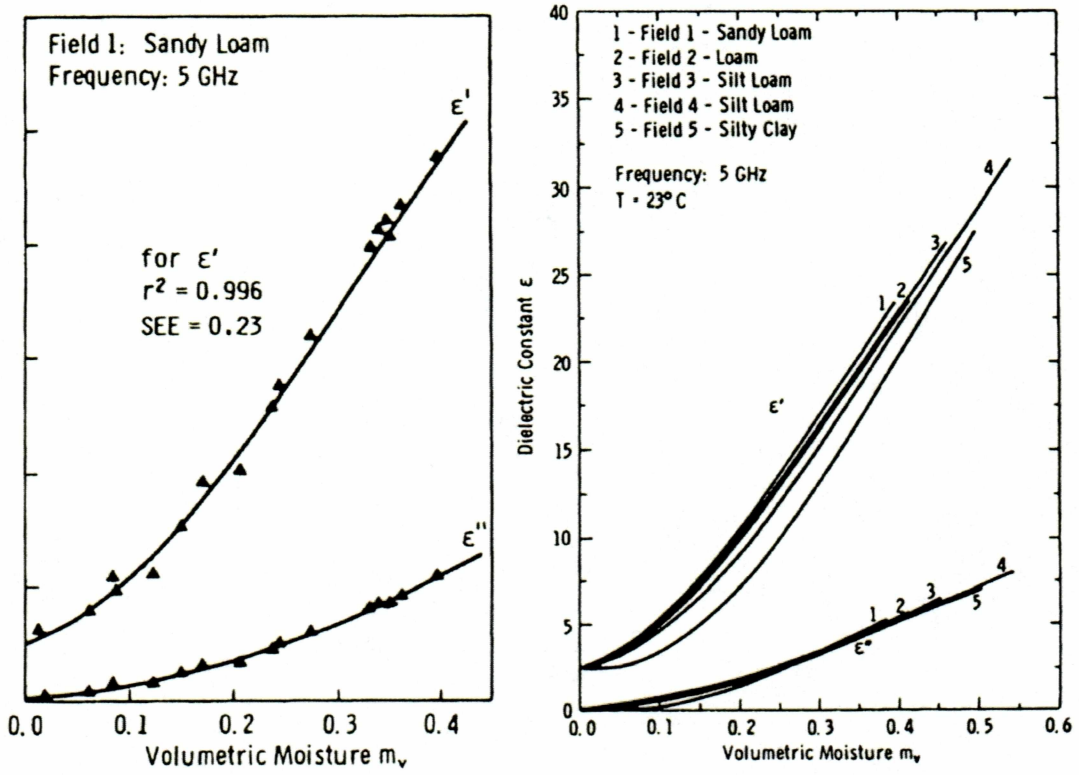

Figure 3.1, a , b, (A, left) The effect of increasing soil moisture on the dielectric constant for soils. (B, right) The effect of soil texture on dielectric constant. (From Hallikainen et al. 1985.)

Table 3.1, The date of freezing and thaw at various North Slope sites.

Location	**Date of Thaw**	**Date of Freeze up**
	2000	
Sagwon MAT		Sept 16th
Sagwon MNT		Sept 11th
Franklin Bluffs	May 31st Sept	14th
Regionally Averaged from weather Stations	June 6th Sept	7th
	2001	
Sagwon MAT	June 4th	
Sagwon MNT	May 28th	
Franklin Bluffs	May 31st	
Regionally Averaged from weather Stations	June 10th	Aug 14th

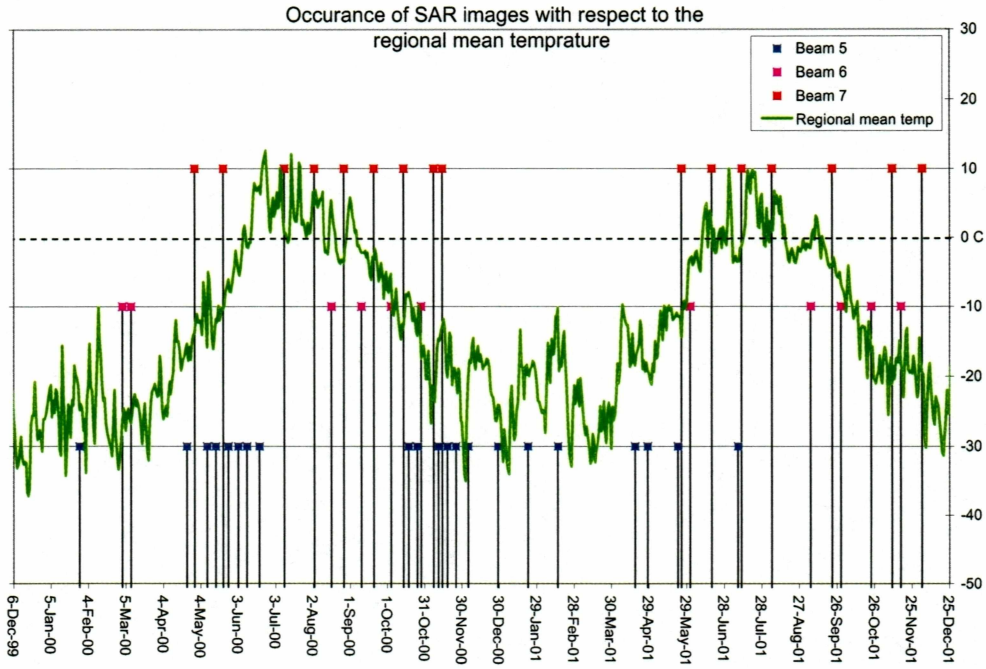

Figure 3.2, The date occurrence of SAR scenes within the two year archive period.

mean backscatter value was calculated for each image. From this analysis there is a pattern of decrease in backscatter by approximately 3 dB when the ground freezes. Table 3.2 shows the breakdown of Sigma 0 backscatter by year and season.

This is consistent with studies of Arctic tundra south of our study area that have been carried out by Rignot et al. [1994] that indicate a drop in backscatter of a minimum of 3 db as the ground freezes, in ERS-1 imagery with a 23° look angle. The geographic region in that study was in an area of significantly higher vegetation biomass, although it is not clear if the biomass has a significant role in backscatter change. The incidence angle of the Radarsat standard beam modes 5-6-7 is from 36°to 49°. Imagery taken with this significantly higher angle has a lower backscattering coefficient (see Figure 3.3), which in turn will limit the range of change that any surface could produce. Wegmüller [1990] indicates that there is a difference in the effect of incidence angle between frozen and unfrozen soils (see Figure 3.4). Despite these effects, an average 3.0 dB change is measured, indicating no weaker backscattering effect in beam modes with higher incidence angles.

The backscatter averages of the images from Standard beam 6, taken during 2001, are the only exception to the expected backscatter of about –16.25 dB during winter, and have a approximate –18.1 dB signal. This is most likely due to two factors: first, the small number of images sampled, and second, the effect of larger moist snow crystals caused by refreezing in one of those scenes.

A Combination of nine images from Standard beam 7 acquired in 2000 indicates a systematic variation in backscatter with respect to the season and other factors. Colour composite images, formed using subsequent scenes stacked into the RGB channels, have the effect of colouring the changes, making the variation easier to distinguish. The six resultant colour images are seen in Figure 3.5. The change in overall hue, from blue to cyan to grey to yellow to red,

Table 3.2, The effect of the freezing of the ground on the radar backscatter brightness. Taken from data of three Radarsat beam modes (standard beams 5,6 and 7), of a consistent study area 60 km by 60 km, centred North West of Sagwon.

Year	Frozen Ground (dB)	Unfrozen Ground (dB)	Sigma 0 relative backscatter (dB) of frozen to unfrozen.
Standard Beam 5			
Combined for 2000 & 2001	-16.3586	-14.0799	-2.2787
2000	-16.5823	13.4353	-3.1470
2001	-15.5198	-14.4022	-1.1177
Standard Beam 6			
Combined for 2000 & 2001	-16.6679	-12.9253	-3.7435
2000	-16.0506	-12.9134	-3.1372
2001	-18.1085	-12.9373	-5.1712
Standard Beam 7			
Combined for 2000 & 2001	-16.1672	-13.1108	-3.0565
2000	-16.4078	-13.4742	-2.9336
2001	-15.6860	-12.8382	-2.8478
Overall			
Beam 5	**Beam 6**	**Beam 7**	**Overall**
-2.2787	-3.7435	-3.0565	**-3.0262**

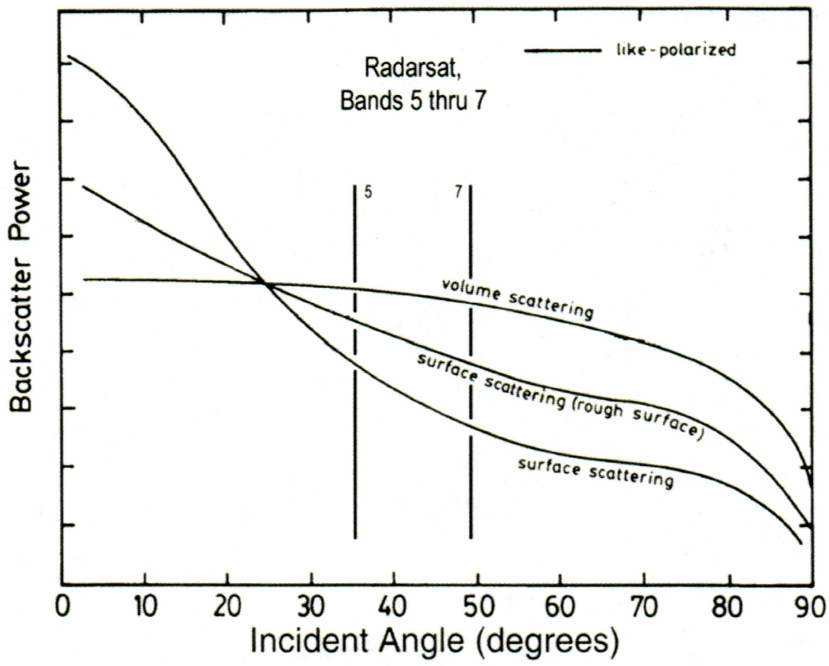

Figure 3.3, The Variation of backscatter power due to incidence angle, the dependence on the surface precludes a empirical removal algorithm achieving a high level of success. After Leckie [1998].

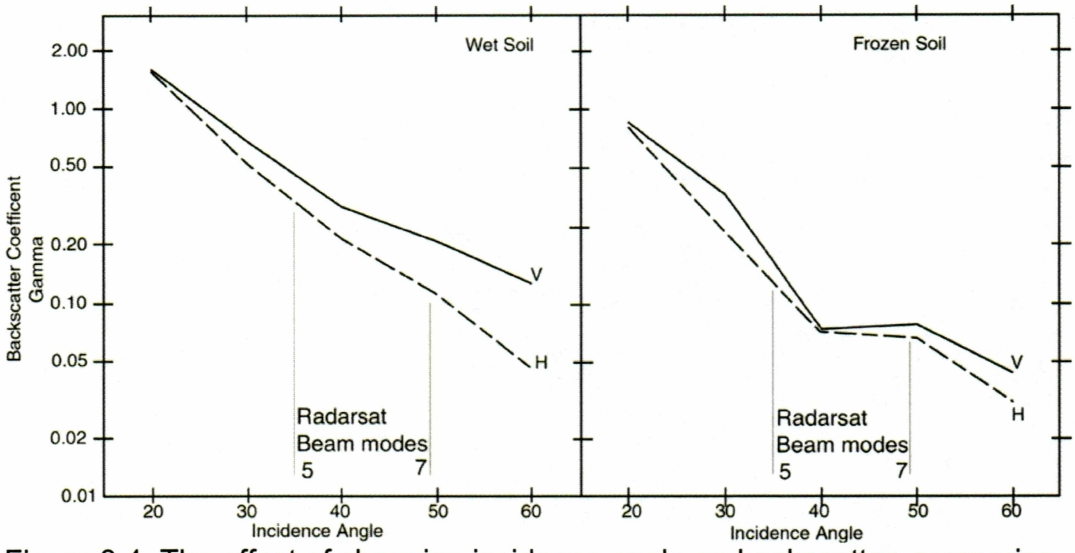

Figure 3.4, The effect of changing incidence angle on backscatter, comparing frozen and unfrozen soil, (after Wegmüller 1990). This change in brightness relationship adds complexity to interpretation of absolute backscatter value changes between scenes from different Radarsat beam modes.

is what we would expect as lower intensity images occur in the early and late parts of the year, when the ground is frozen.

The area shown in the images of Figure 3.5 is centred on Sagwon, and an enlarged view is show in Figures 3.6. which gives an indication of the topography and identification of the strong radar reflectors in the area. Figure 3.7 illustrates the systematic change of backscatter from scene to scene, as a result of the annual cycle.

The winter scenes have a significantly lower backscatter than the scenes acquired when temperatures were above freezing. This can be clearly seen in Figure 3.5 and 3.7, (A) in which the ground is frozen in all three scenes, though recrystallisation of ice has increased the return of the May scene and in (B), where the ground is frozen in the first two scenes, both scenes exhibiting a strong blue hue. Warmer ground temperatures of the later scenes are indicated by frozen lakes in both the April scenes, which are yellow (red + green) in A and just red in B, indicating that they were unfrozen by the 22nd of May, though this is complicated by floating ice having a higher backscatter [Jefferies et al. 1994]. Figures 3.5 and 3.7, (C) show approximately uniform brightness of thawed soil in all three channels giving a grey overall colouring. In (D) the brightness of the scenes from August are strongest, due to the increase in backscatter from vegetation. This agrees with a Normalized Difference Vegetation Index (NDVI) derived from AVHRR imagery (shown in Figure 3.8) that indicates the strongest vegetation derived signal from the first two weeks of August, See also Figure 3.9.

The scenes from late in the year (E, F) strongly illustrate the lower backscatter brightness of images after freeze-up, with E have a yellow hue, indicating little input from the 20th September Image and in F, strong red hue showing continued low backscatter values in the October image.

The effect of melting snow is very complicated and has a strong effect on backscatter. It can be seen very clearly in Figure 3.10. Scenes like these were

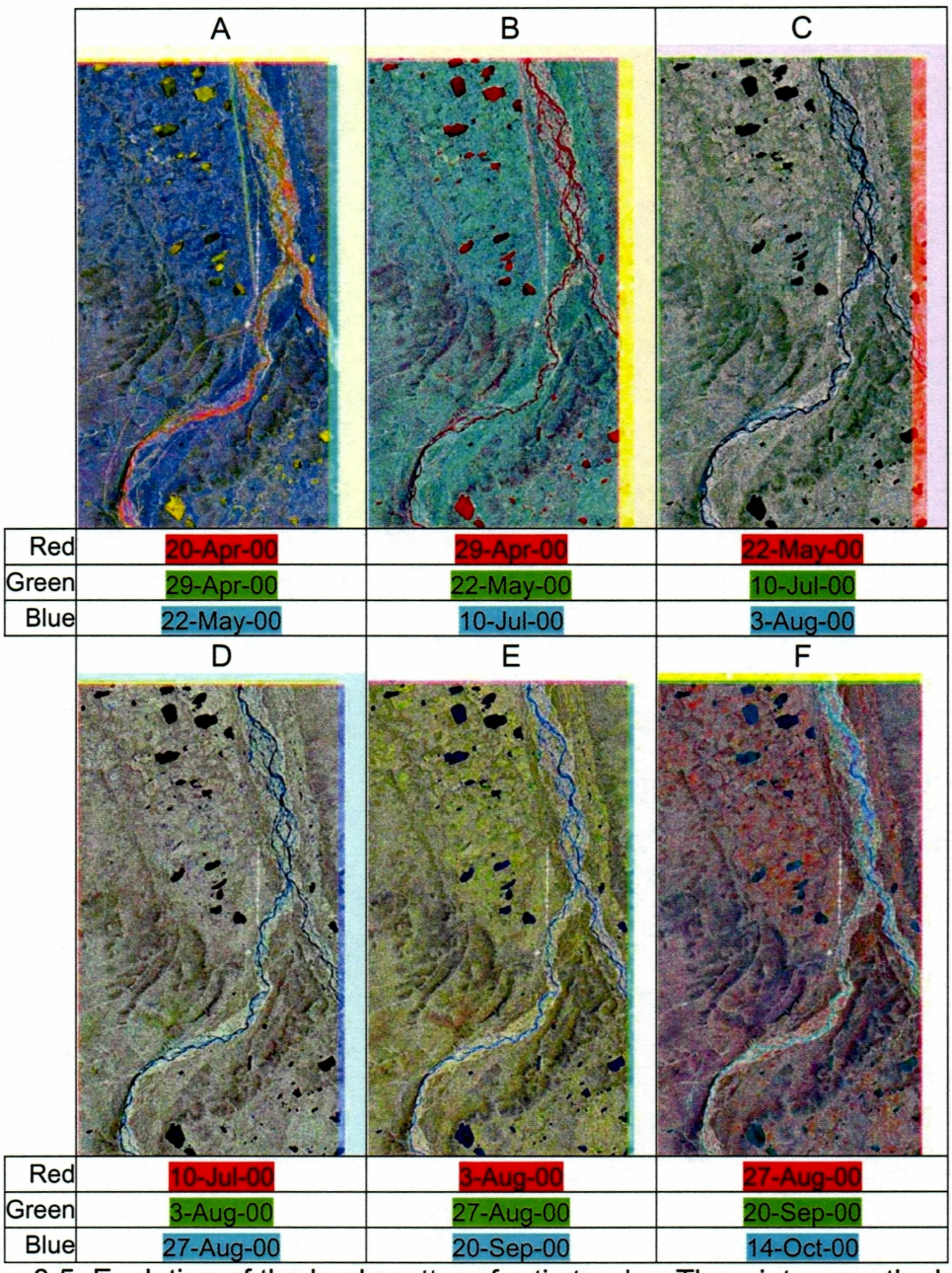

Figure 3.5, Evolution of the backscatter of artic tundra. The winter months have a lower backscatter return on average (images 1,6 being darker). In (A) the May image (blue) dominates colouring the whole scene, giving it a blue tinge and the bottom right image (F), has a strong August channel (Red), and a corresponding red tinge.

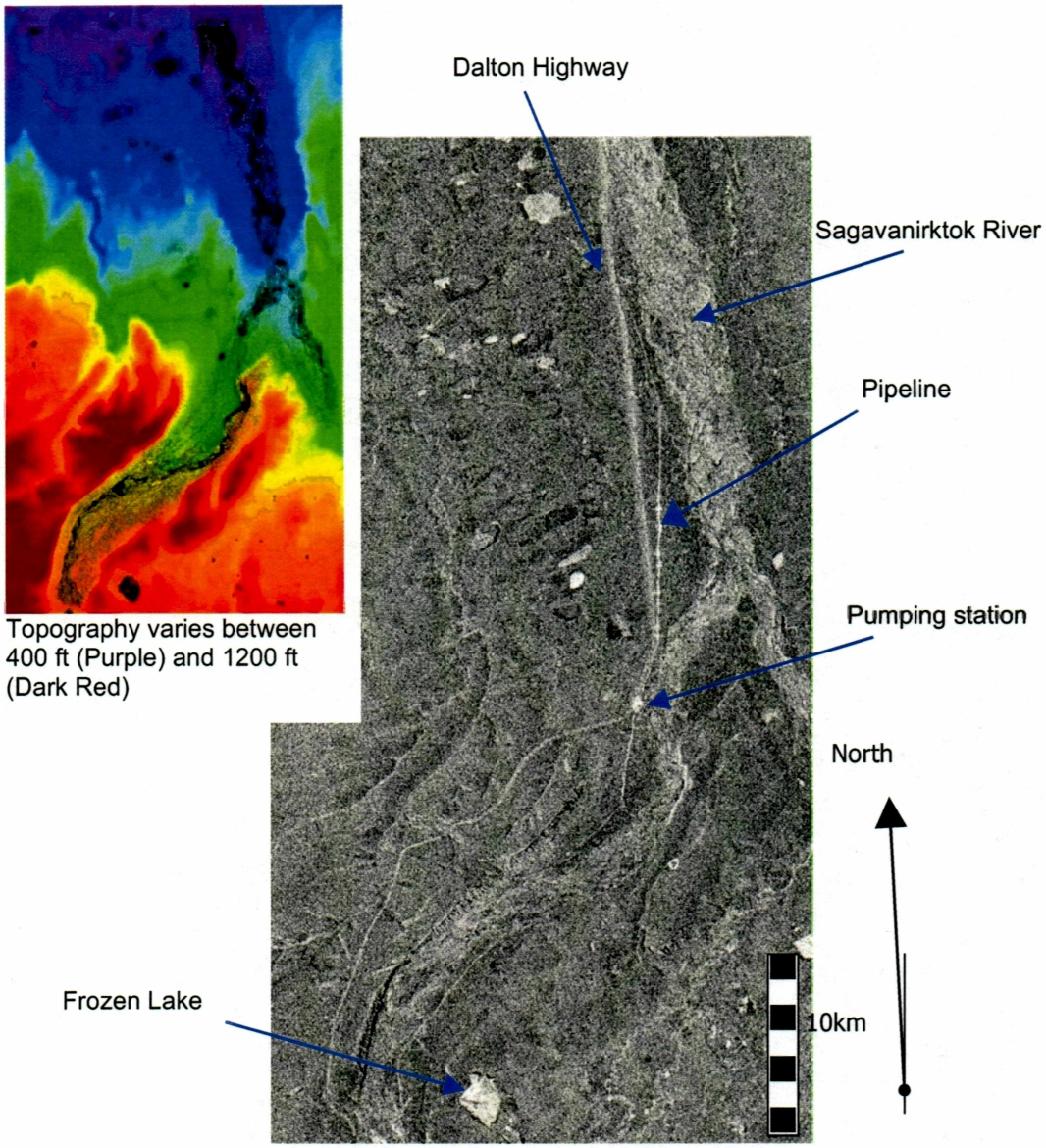

Figure 3.6, Enlargement of the Sagwon Region, Showing the Dalton highway running North South in the centre and the Alaska pipeline pumping facility. A terrain-corrected, calibrated beam-mode 7 Radarsat image. Scene is 30 km by 56 km. Topography of the same region is shown at the top right, with the river and significant lakes shown in black.

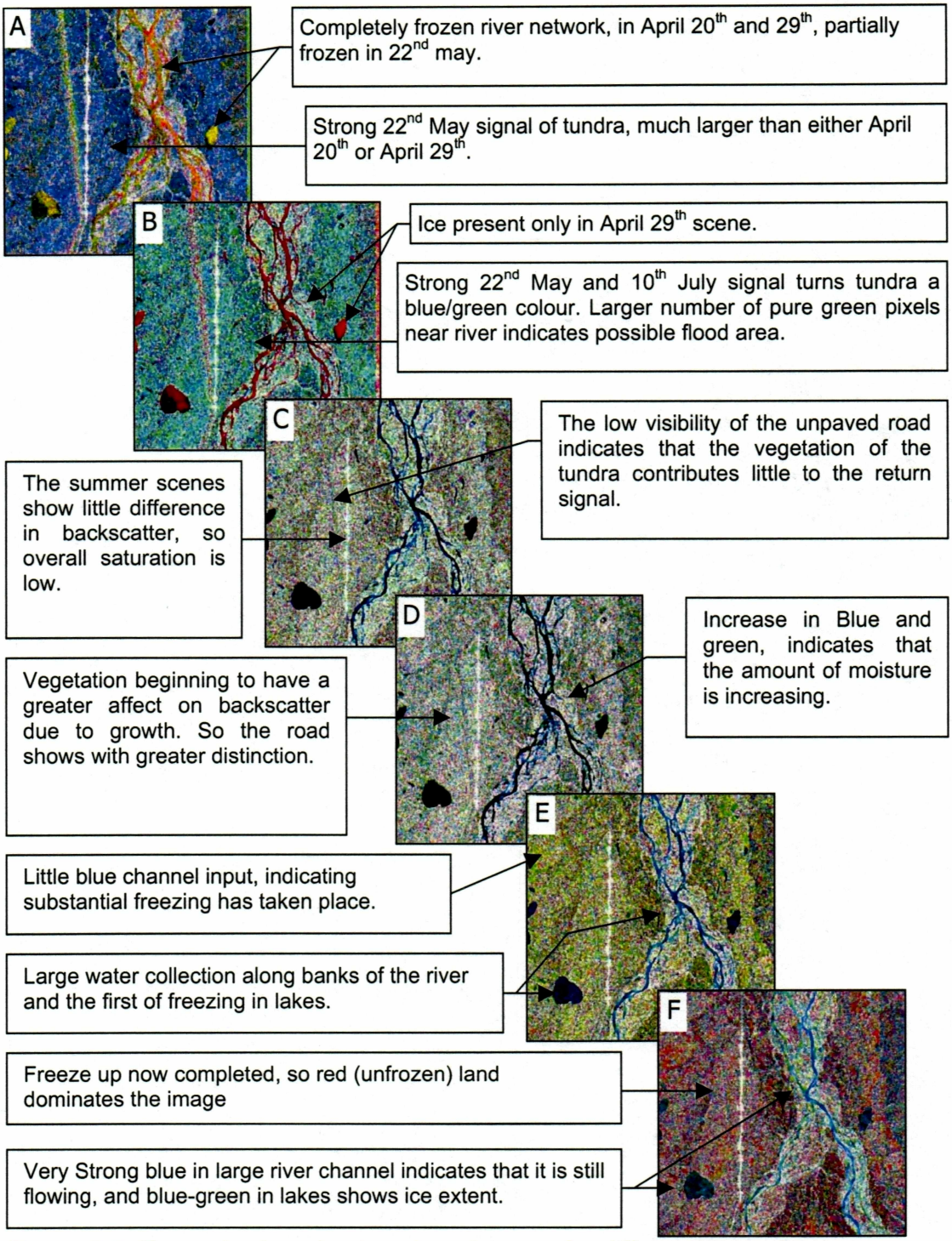

Figure 3.7, Examples how backscatter changes for different ground cover over time, and the strong effects of moisture, freezing and vegetation change.

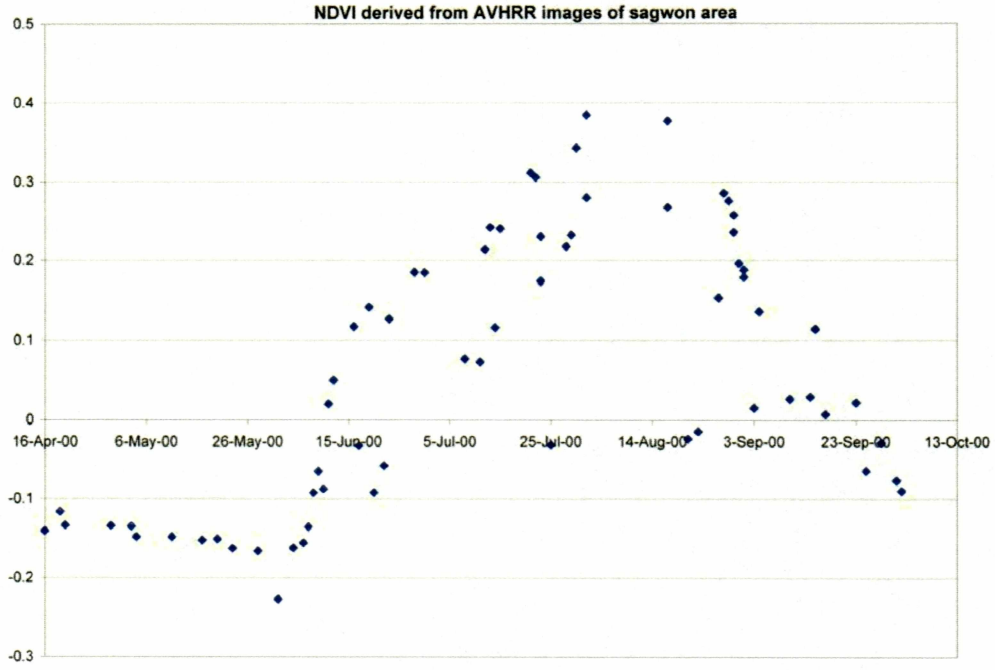

Figure 3.8, The variation of average NDVI of the area over Sagwon (shown in the next Figure), images with a partial cloud input show a slight decrease in NDVI, images with a snow layer show a strong negative index. The NDVI index agrees with field observation that snow cover began to decrease near the 4th of June and was largely gone by the 11th.

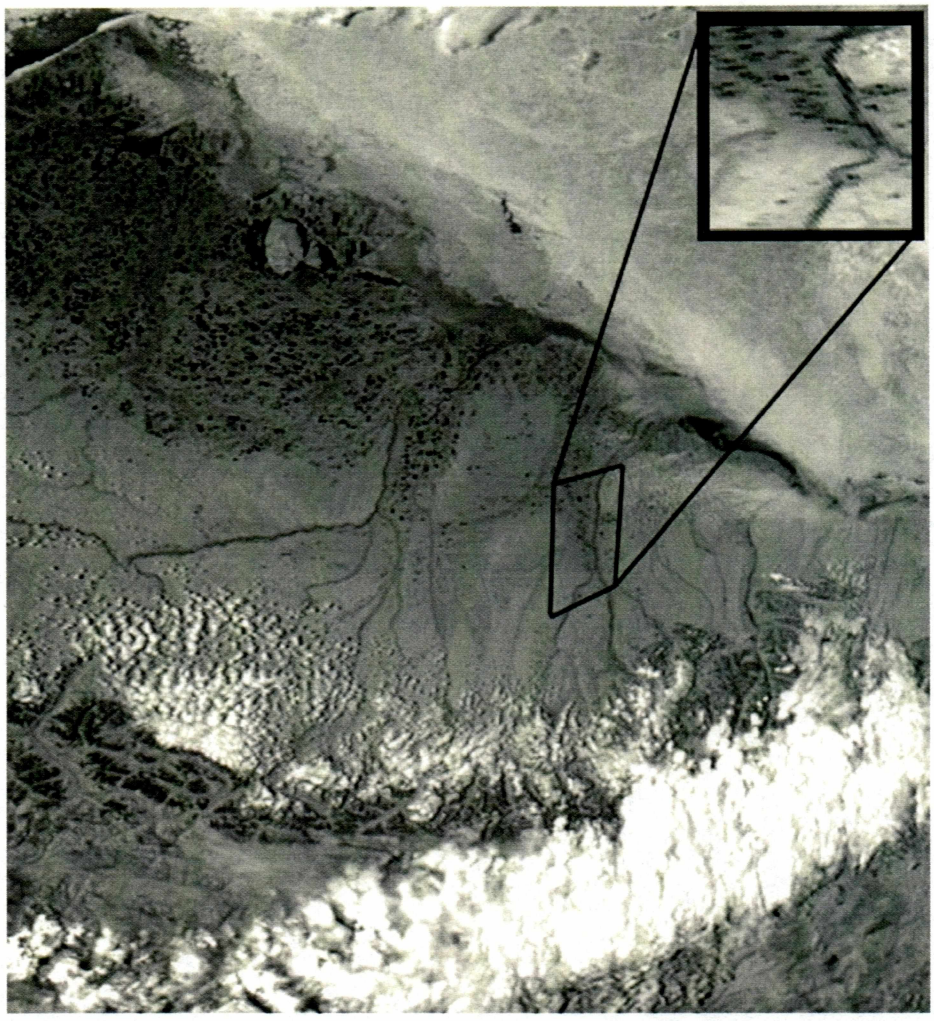

Figure 3.9, An AVHRR image from the 13th July 2000, showing (as insert) the Sagwon region, the mean value of all the cloud free pixels was used for NDVI calculations.

excluded from the backscatter analysis. The attribution of the strong loss in backscatter strength in Figure 3.10 to the presence of melting and wet snow is supported by the AVHRR NDVI data which indicates snow melt taking place from the 4th to the 11th of June in the Sagwon Area. Figure 3.11 shows the progression of the melt front in one of the AVHRR images. AVHRR has 1 km pixels at NADIR, so it is likely that there is still appreciable snow in the snow free area. However, the bulk signal is enough to delineate an approximate snow/snow free boundary. The 4th of June image is consistent with field observations that indicate that most snow was fully melted by that date.

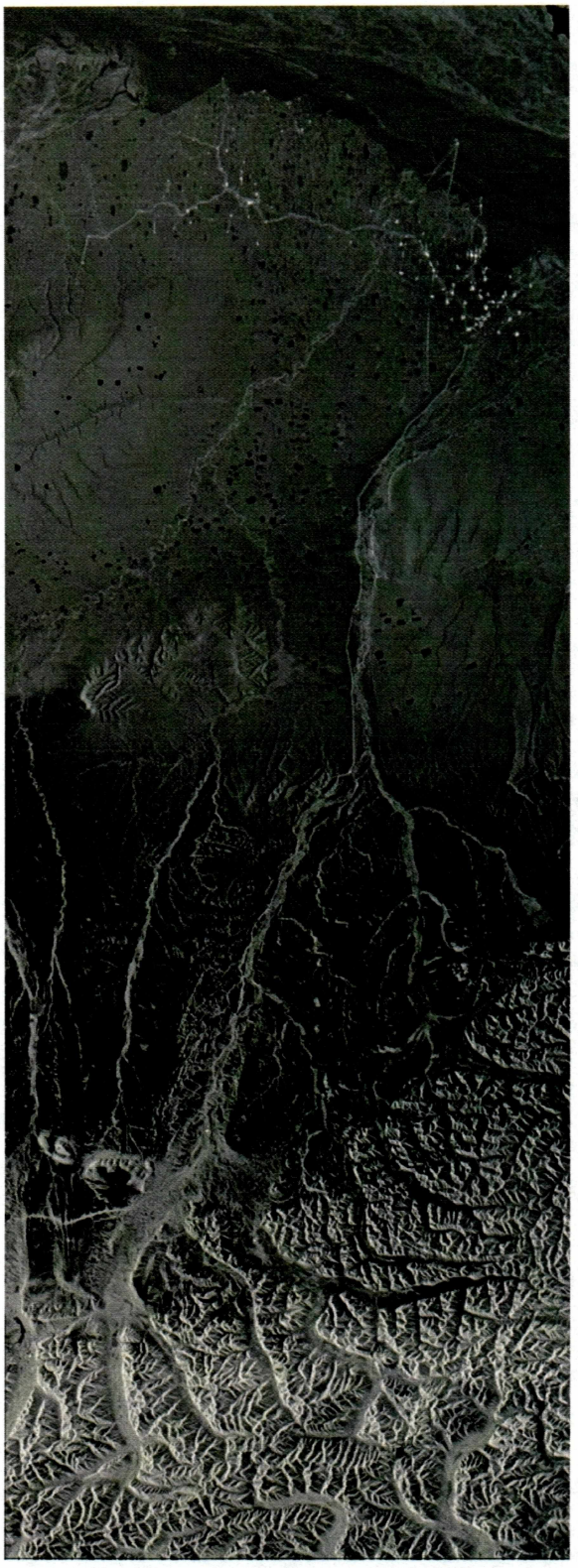

Figure 3.10 , The effect of wet snow, this Radarsat Beam 5, image was taken on June 3rd 2000, as melting of the snow layer was beginning to take place. Darker areas are places with a higher amount of unfrozen water in the snow pack. Further north, where the snow was still frozen there is a stronger backscatter signal.

The drill sites and equipment of the Prudhoe Bay oil field show up as bright points, as does their network of ice roads and pipelines.

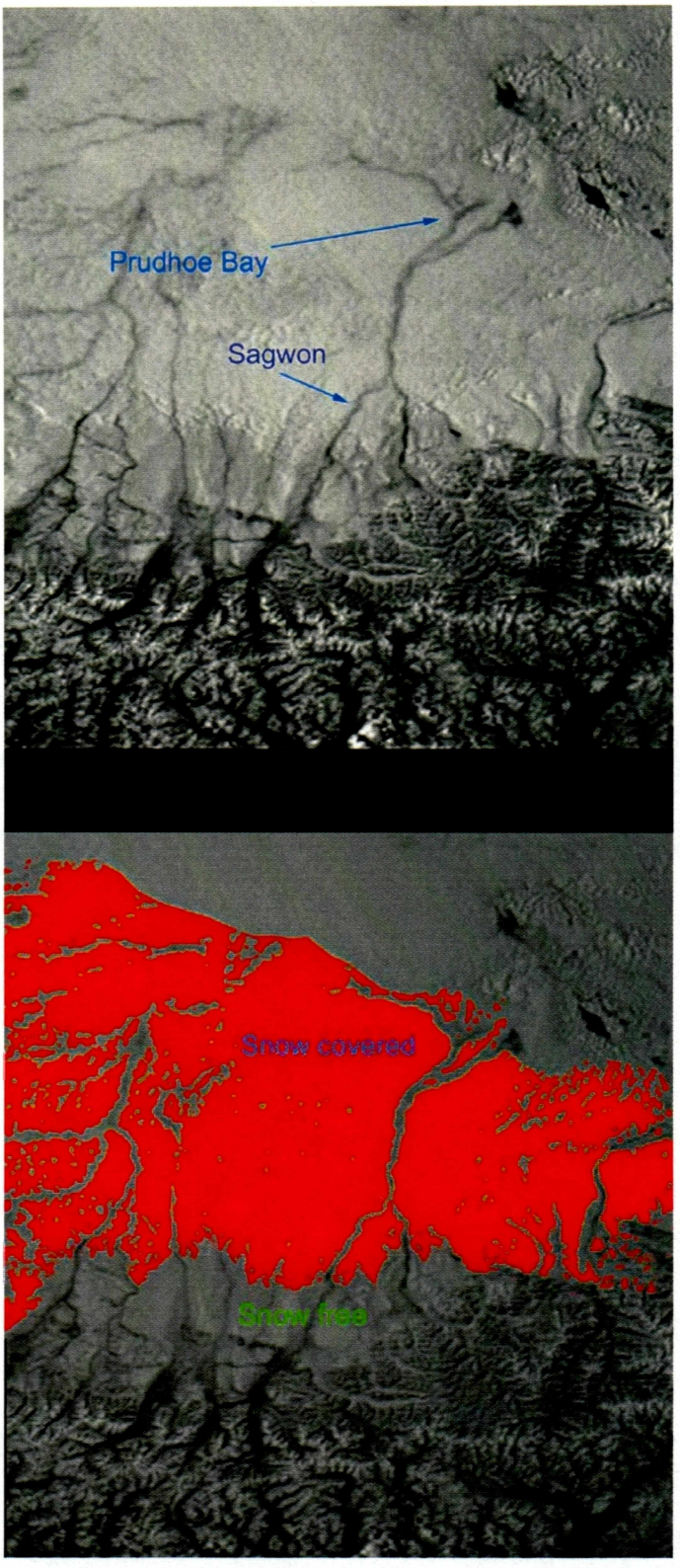

Figure 3.11, This AVHRR channel 2 image, taken on June 4th, shows the progression of the snow melt (red). Brighter melting snow-covered regions were thresholded and coloured red to highlight the boundary.

The Use of Empirical Orthogonal Functions on Radarsat SAR scenes to map tundra type.

Previous studies of vegetation and land cover of the North Slope region of Alaska have classified plant species [Muller et al. 1999], which can be then divided between species predominantly found in moist acidic tundra environments (MAT) to the south and those of non-acidic environments (MNT) to the North [Walker et al. 1998]. Moist acidic tundra is characterized by a greater amount of vegetation and a thicker and more continuous organic soil layer. Areas of non-acidic tundra have a greater mineral input in their surface soil layer [Bockheim 1998].

The technique of Empirical Orthogonal Function (EOF) analysis is also known as Principle Component analysis when used on non-temporal data, and also as singular value decomposition, and is derived from the Karhunen-Loève expansion [Everson et al. 1995]. The use of empirical orthogonal function techniques on a time series of SAR scenes from Radarsat requires the geocoding and coregistration of all the scenes within a beam mode. Each input scene was also down sampled to give 100 m by 100 m pixels to allow more rapid processing. Then the images from each beam mode were stacked and analysed independently.

The expression of EOF analysis is based upon *Everson et al.[1995]* and *Eslinger et al. [1989].* The temporal fluctuation of the value of the radar

backscatter about the mean backscatter at a single geographic point (x), can be denoted by $\Phi(x,t)$; EOF analysis expresses this point as an expression on the EOFs φ_n:

$$\phi(x,t) \approx \sum_{n=1}^{N} a_n(t)\varphi_n(x) \tag{1}$$

The modal coefficients $a_n(t)$, and the empirical orthogonal functions (eigenfunctions) $\varphi_n(x)$ are determined from minimizing the error over N such that

$$< \int dx \left| \phi(x,t) - \sum_{n=1}^{N} a_n(t)\varphi_n(x) \right|^2 > \text{ is minimized,} \tag{2}$$

and the functions that fulfil this criteria force $\varphi_n(x)$ and $a_n(t)$ to be orthogonal and completely described by the dataset concerned. The modal coefficients or eigenvectors can be expressed as :

$$< a_n(t)a_m(t) > \;=\; \lambda_n \delta_{nm} \;=\; < \left(\int \phi(x,t)\varphi_n(x)dx \right)^2 > \tag{3}$$

Each eigenvalue λ_n is the square of the projection of the image taken at time t onto the n^{th} empirical eigenfunction. EOF analysis results in three image groups (one for each beam mode). Each has a number of scenes (components) created from the original data set; these components express the temporal variance of amplitudes within the source images. A components Eigenvalue indicates the relative amount of variance expressed within the beam mode. Each component scene is constructed through the summation of the amplitude images

multiplied by a set of associated weights, known as the eigenvectors. Each component successively describes a smaller degree of input scene variance.

The first few components of each beam mode express the variation in overall scene brightness due to the slight difference in the ground footprint between scenes. This is caused by two reasons, fluctuations in the precise orbits of the satellite, and the slight effect of inaccuracy in the inter-scene correlation as a result of its local misalignment to within a few pixels. Lower components begin to show regional features of the data itself and through analysis of the relative eigenvector weightings of each input scene we can establish their cause.

The boundary between acidic and non-acidic tundra is visible in all three Radarsat beam modes, though at different component levels. Figure 4.1 shows the boundary in the three beam modes highlighted in red, and Figure 4.2, (the three corresponding eigenvector weightings,) as well as the surface temperature time series in both the MNT and MAT.

The eigenvector weightings within the component images that show the MNT/MAT boundary are only strong in the winter amplitude image, (see Figures 4.2, and 4.3) which is confirmed in an inspection of the raw amplitude images (see Figure 4.5). An inspection of all the images showed that in no single image is the boundary between MNT-MAT unambiguously visible.

The eigenvalues assess the amount of variance that the component explains. Our components that show a MNT-MAT boundary have eigenvalues

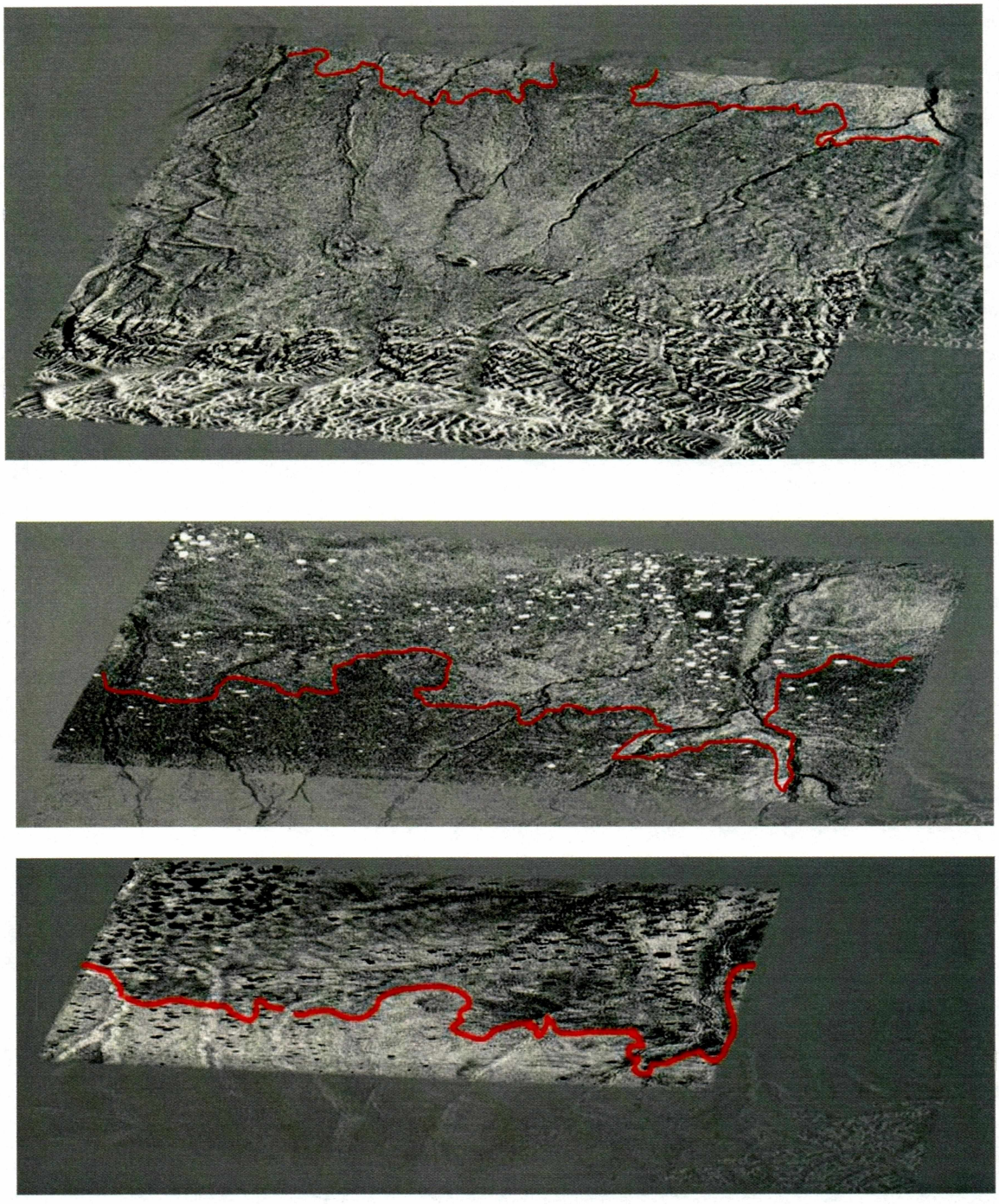

Figure 4.1, From Top to Bottom, Radarsat beam mode 5,6,7 component images 5 of 23, 7 of 11, 1 of 9 respectively, each showing the boundary between MNT (above red line) and MAT (bellow red line) tundra.

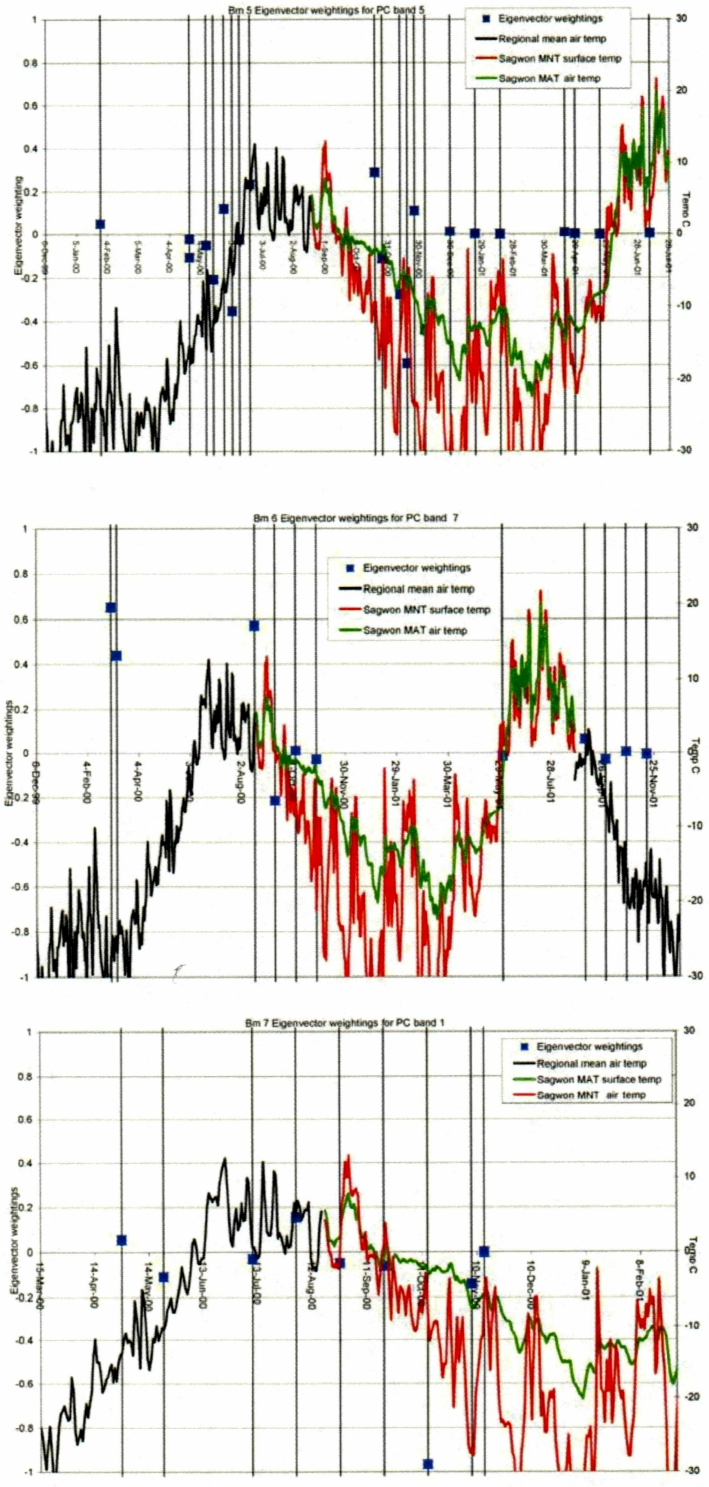

Figure 4.2, From Top to Bottom, Radarsat beam mode 5,6 and 7 with component images 5,7,1. Showing the eigenvector weightings required. Strong negative weightings for winter scenes will make the MAT appear darker, Strong positive weightings will make it appear lighter. Overlain is the temperature time series indicating when the ground surface is frozen.

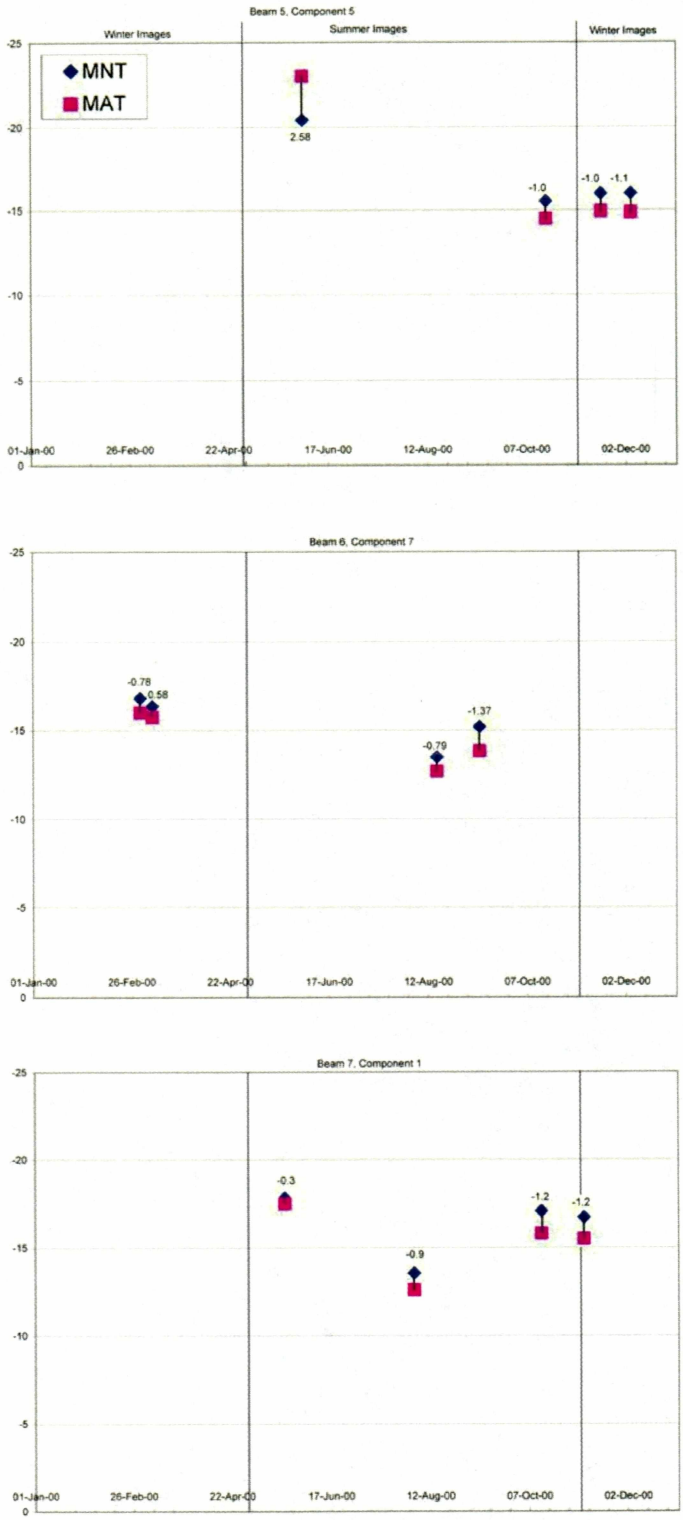

Figure 4.3, The 4 most important eigenvector weightings for each of the three beam modes, with a on average larger difference between MNT and MAT brightness values in the winter period.

The backscatter difference between MAT and MNT in summer is 0.94 dB. in winter this difference is 1.00 dB.

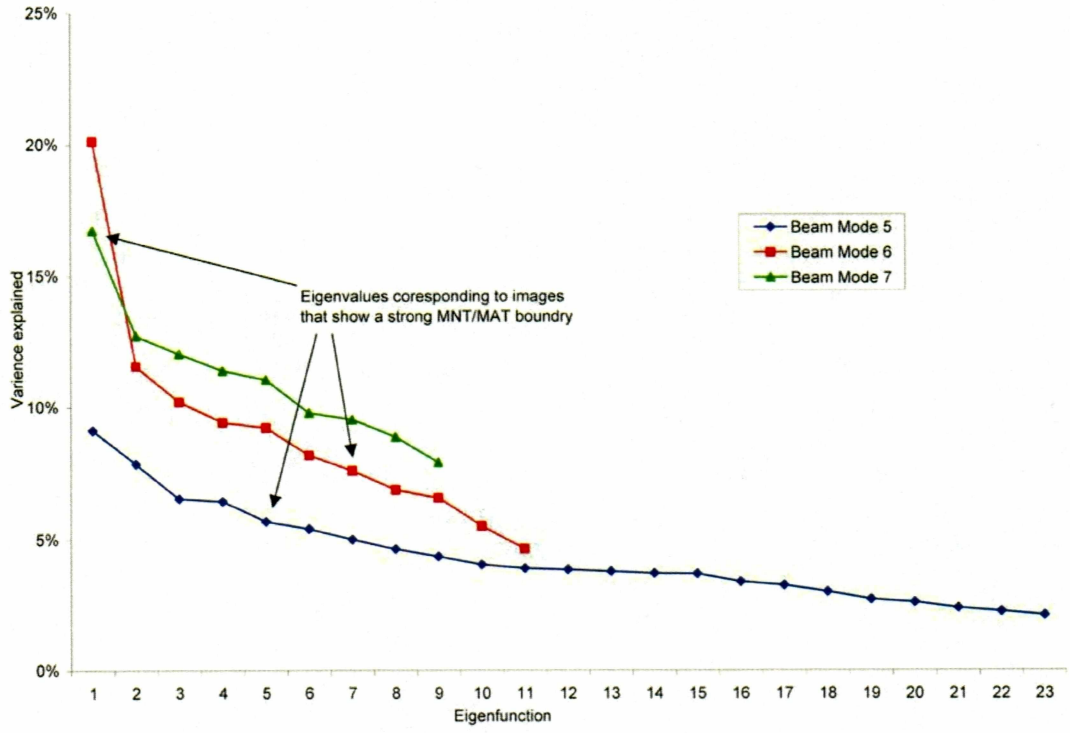

Figure 4.4, The eigenvalue ratings across all three beam modes, and the percentage variance that the image explains.

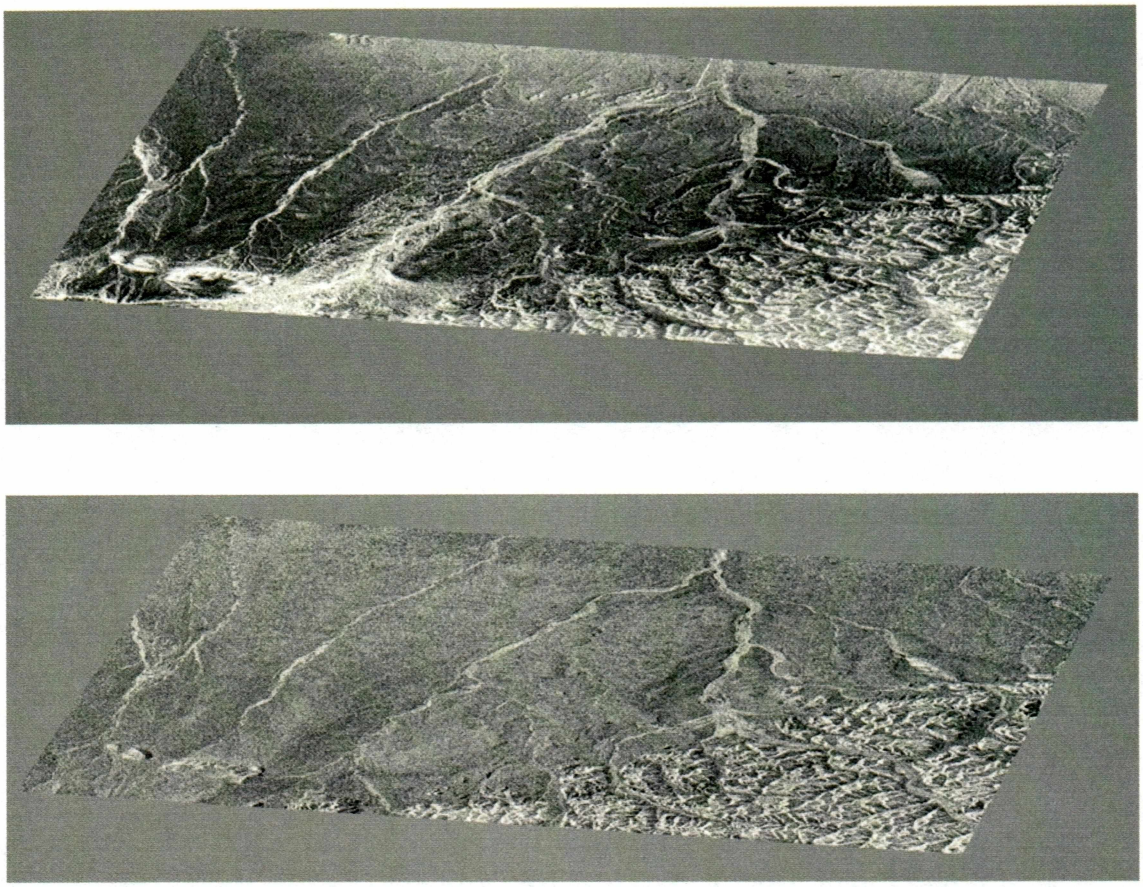

Figure 4.5, Two Images from beam 5, top from summer (3-Jun 2000) showing no clear boundary with a eigenvector weighting of -0.35 and Bottom image from winter (18-Nov 2000) showing a slightly more clear MNT/MAT boundary.

that occur within the top few components, indicating that though not the most prominent feature it does still have a strong brightness variance associated with it, (see Figure 4.4).

In the case of beam mode 5, the study area does not completely fall within each scene acquired. The higher eigenfunctions are dominated by expressing the variation in geographic coverage that a greater number of scenes fully cover. High frequency noisy speckle components explain from component 9 downwards. The fact that we see the boundary in component 5, well above the onset of noise-dominated components is encouraging, as it illustrates the strength of this feature is well above that of any noise component.

A similar situation persists in Beam mode 6; components 1 through 4 express the changing geographic coverage between scenes and the MNT/MAT boundary is just visible in component 5, though very close to edge, it is most distinct in component 7 because that component deals exclusively with the variance within the areas of data. Components 9 through 11 deal with the higher frequency noise components indicating that the boundary is well above this level in terms of statistical significance.

Beam mode 7, in contrast, has the study area within all the sample images, though the consistency of the footprint of each radar scene is similar to the other beam modes, and this in turn shows the boundary in the first

component, in addition high frequency noise components are not present until the 6th component.

A feature of our radar scene archive is that it does not exhibit a strong drop off in eigenvalues (% variance explained) with their lower components (see Figure 4.4) when compared to some data sets traditionally analysed with this technique. This indicates a more even distribution of variance within the scene, and no strongly dominant variance producing sources. This in turn can be linked to the consistency of geographic footprints between images. The beam 7 image archive has a significantly higher proportion of images covering a similar geographic area than the beam 6 scenes and in turn beam 5 images. It is this factor that seems to control the positioning of the MNT/MAT boundary within the EOF components, and the amount of variance each individual component explains. Selecting the dataset with a more consistently scene populated geographic region would raise the component EOF containing the boundary to a component that explains a greater proportion of the variance, but it would not increase the strength of the boundary in the images.

When a EOF Radarsat image is compared with an optically-derived image showing the boundary between MNT and MAT, a high degree of correlation exists. Figure 4.6 shows a MODIS-derived image that takes advantage of the difference in leaf area between the two regions to highlight their boundary. This image is formed from a 5-3-1 composite, and the same MODIS image, after

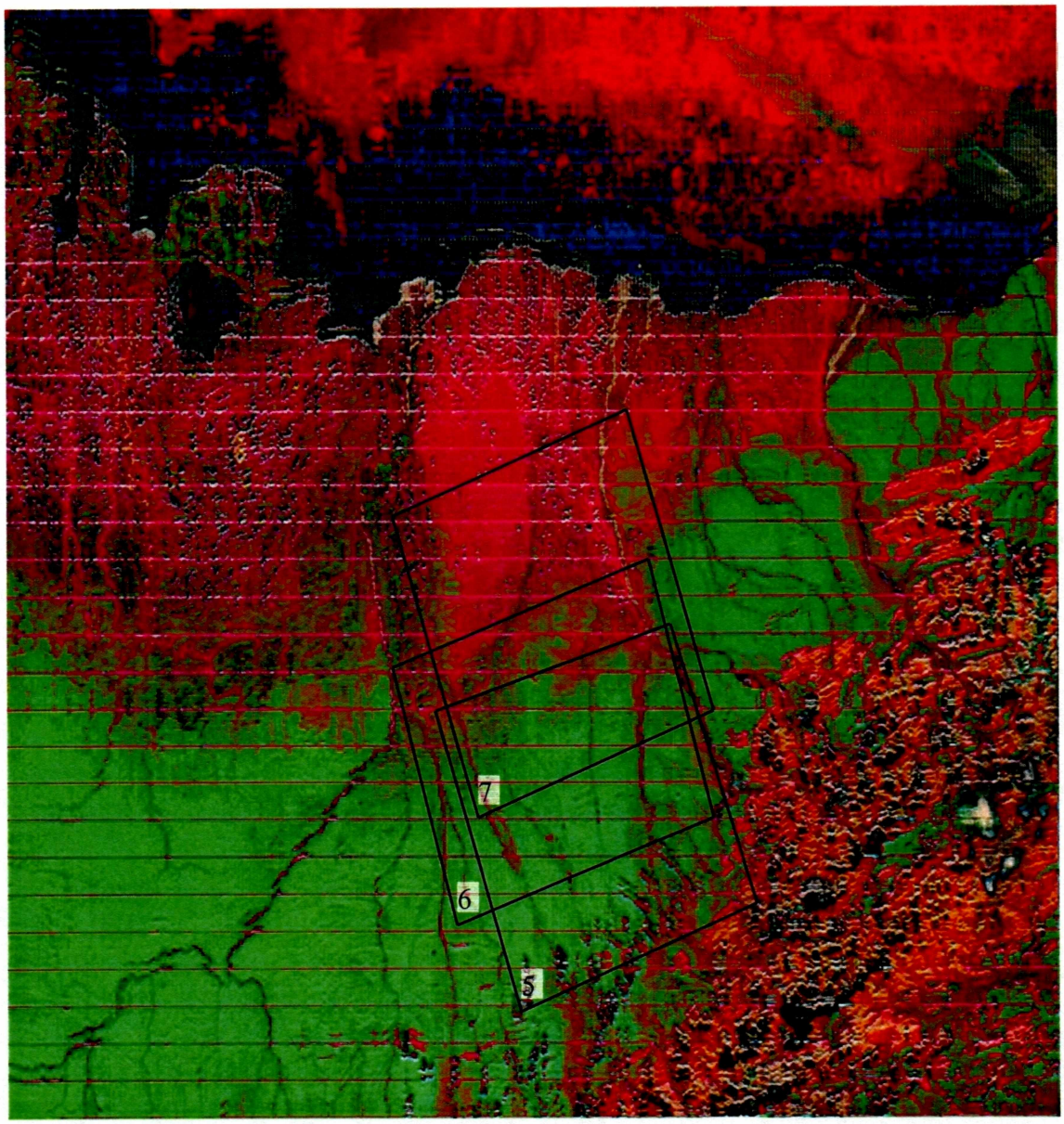

Figure 4.6, A July 2002, MODIS image of the Kuparuk River Basin Alaska, 5 3 1 false-colour composite, overlain in red with a principle component image (component 4) to show the boundary between MAT (green) and MNT (Red). The study region is outlined for each of the beam modes.

Principle Component analysis, with component 4 thresholded and taken as an overlay to highlight the MNT-MAT boundary. The fewer vegetation leaves of MNT appear in red and the larger number of leaves in MAT appear green. Figure 4.8 shows the same MODIS image overlain on a EOF Radarsat beam mode 6 component 5.

The complexity of the tundra environment suggests that no single factor can explain the reason for the boundary being visible in the amplitude images. A function of EOF analysis is that it will only isolate images in which the variance is exhibited with statistical completeness. If three images fully describe the variance, then even though similar information may be present in other images, this fact will not be represented in the eigenvectors weightings. Therefore, a manual examination of the raw images is required to identify which images exhibit a particular feature. Figure 4.7 shows that no boundary is seen in scenes acquired during the summer (May to November), and this absence of boundary indicates that the difference in backscatter brightness between MNT and MAT is related to winter processes or features.

Ground vegetation plays a role in the backscatter properties of the tundra. The greater the thickness of vegetation, the greater the backscatter signal and the brighter the backscatter image. If the vegetation is deciduous, then that will cause a temporal change in backscatter, with the loss of leaves causing a lower backscatter signal. The freezing of liquids within vegetation has the effect of

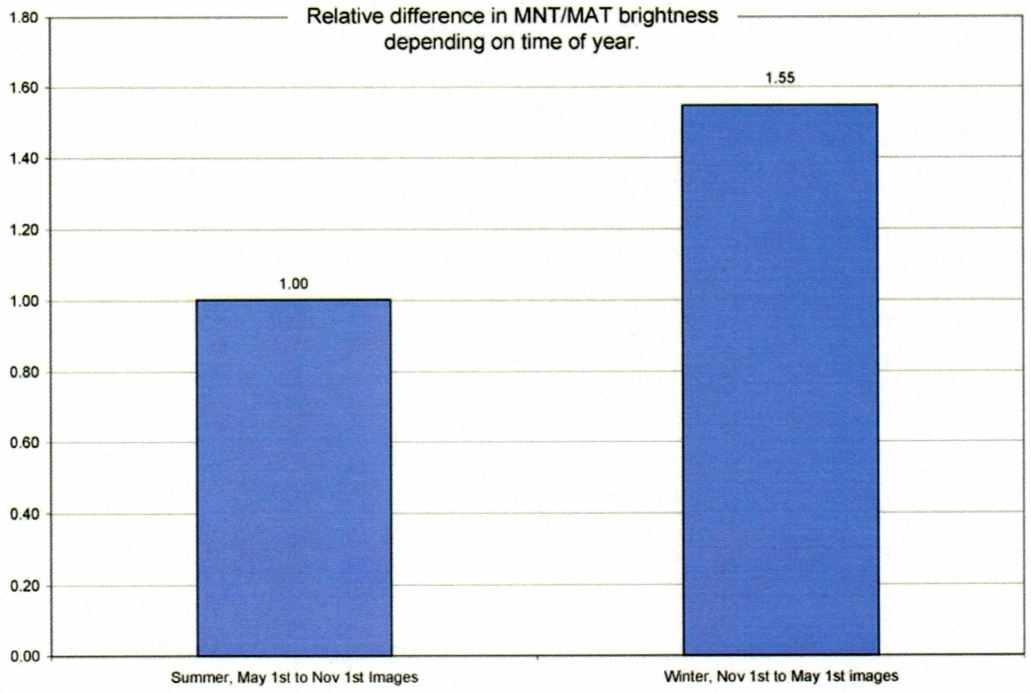

Figure 4.7, A comparison of the difference in backscatter brightness, using the ratio of MNT to MAT regions broken down into summer and winter periods, across all images and beam modes.

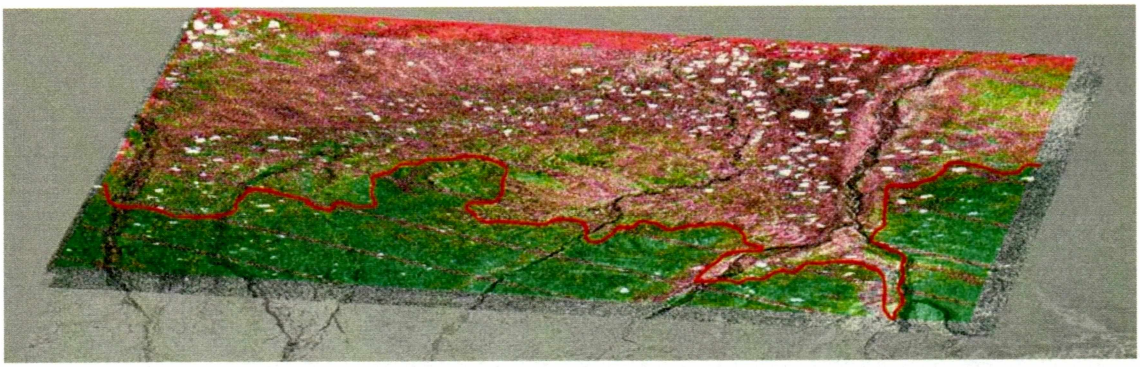

Figure 4.8, A false colour MODIS image (PC enhanced), highlighting MNT (red) MAT (green) overlain on a EOF Radarsat beam mode 6 component 7 image, showing a high degree of correlation between the sources.

reducing backscatter as well. Unfrozen bare mineral earth has a strong backscatter signal, which strengthens with increasing water content. The effect of freezing water in the soil strongly reduces backscatter, especially for coarser grained soils.

The lack of boundary in summer images indicates that in the Arctic tundra it is not possible to see the MNT/MAT boundary due to a leaf area change in C-band radar images.

As noted in the previous chapter, the presence of snow on the ground has a complex interference effect on the radar signal, with the top surface, volume of snow and ground snow interface all contributing to the backscatter signal. If the snow is characterised by large dry grains, then the snow will have a relatively strong backscatter signal. The strength of backscatter will fall off with decreasing grain size and increasing wetness.

Numerical work by Koskinen et al. [2000], shows that for a snow layer of 1% wetness and 1 meter thickness all soil backscatter return can be lost, hiding both areas of low backscatter return and rough areas with a slightly higher backscatter. In the Arctic tundra, where snow thickness of 50 cm is not uncommon, and an increase in shrub height has a strong corresponding effect on increasing the snow thickness [McFadden et al. 2001], it is then reasonable to infer that this thicker snow layer would in turn affect the backscatter signal from the tundra. MAT has a greater number plants and a higher plant canopy [Walker

et al. 1998] resulting in a on average thicker snow layer and consequently to a significantly lower backscatter return signal as a result of the snow causing increased volume scattering.

The complicated effect of the snow layer, however, is unlikely to be consistent and large enough to account for the whole backscatter return signal, especially when the thickness of snow is taken into account; as a result, the surface soil layer will also have an effect on backscatter. Figure 4.9 shows the variation in soil surface texture along the Dalton Highway, from north to south (personal communication Dr. Chien-Lu Ping). The transition from MAT to MNT results in an increase in the ratio of sand to clay. A thicker organic layer and increased vegetation would produce a more clay rich medium through pedogensis.

Analysis of the refraction index behaviour of clay and sand with a variety of different water contents and under various temperatures has been carried out by Mironov et al. [2000], showing that the refraction index of sand drops much faster with decreasing temperature than in clay, and this effect is increased with increasing water content. A decrease in refraction index corresponds to an increase in absorption. Areas with a lower clay to sand ratio (MNT) exhibit a lower backscatter return when compared to their above freezing state. In contrast the areas of higher clay-to-sand ration (MAT) exhibit a greater backscatter return and less change from their above-freezing state.

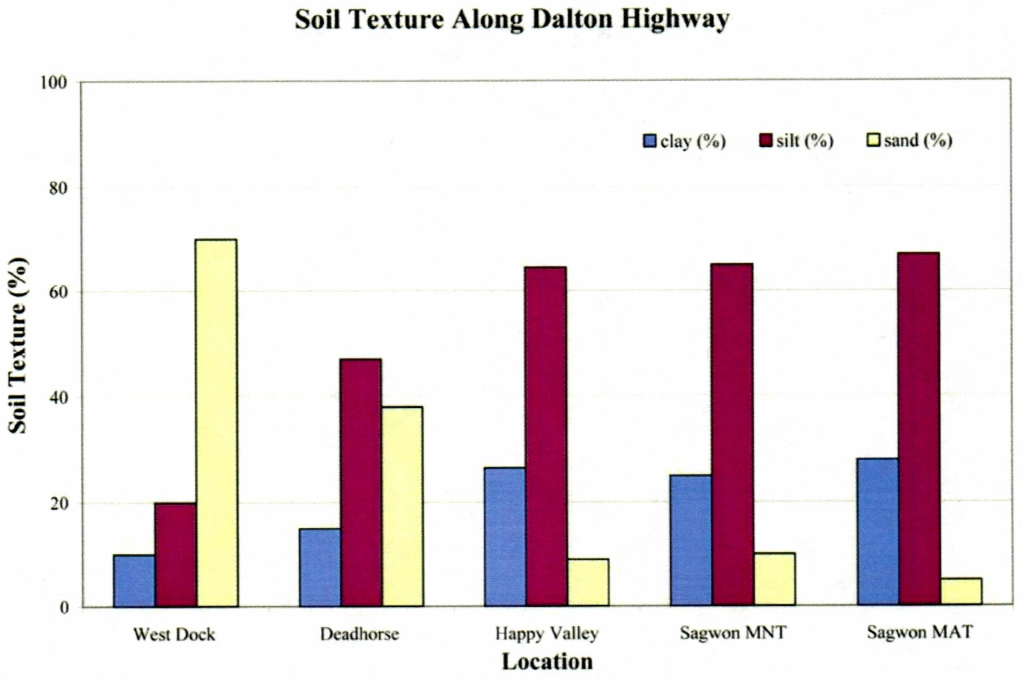

Figure 4.9, The Variation of soil texture from the North (West Dock) to the South (Sagwon MAT), with a systematic decrease in Sand sized particles and a increase in clay sized particles.

This effect is increased by the thermally insulating effect of the thicker MAT snow layer [Walker et al. 1998], which can be seen in Figure 4.2, and the effect of a increased relative soil moisture (spatially from MAT to MNT), during freeze up results in a very slight increase in backscatter values from areas of MAT to MNT.

Active Layer behaviour using DINSAR and Coherence images

Through the use of phase information of radar signals it is possible to derive ground topography. Two coherent radar signals have a phase difference for each point of ground information. Theoretically, the coherence of two radar signals can be calculated as

$$\gamma = \frac{< s_1 s_2^* >}{\sqrt{< s_1 s_1^* >< s_2 s_2^* >}} \quad (1)$$

where

$< ... >$ denotes expectation value

* indicates a complex conjugation operator

In practice this coherence is calculated using

$$\gamma_{total} = \frac{\left| \sum_{k=1}^{N} z_{1k} z_{2k}^* \right|}{\sqrt{\left| \sum_{k=1}^{N} z_{1k} z_{1k}^* \sum_{k=1}^{N} z_{2k} z_{2k}^* \right|}} \quad (2)$$

with N taken to represent a small localized sample of pixels

Areas of high coherence have, by their definition, a lower phase noise. Conceptually the phase of the interferogram is given by,

$$\phi_{\text{int}} = \phi_{Topography} + \phi_{Displacement} + \phi_{Atmosphere} + \phi_{Noise} \quad (3)$$

with the topographic component defined as

$$\phi_{Topography} = \frac{4\pi B_{\perp}}{\lambda R_1 Sin\theta} \left[\Delta h + \cos\theta \Delta R \right]$$

$B_{\perp}$=Perpendicular Baseline

λ=Wavelength (4)

R_1=Slant Range in the first image

Δh=difference in elevation

θ=Incidence angle

ΔR=change in slant range at the two times of imageing due to topography

The displacement/deformation phase can be expressed as

$$\phi_{Displacement} = \frac{\delta R 4\pi}{\lambda} \tag{5}$$

δR = the displacement in the direction of the radar line-of-sight

The SAR-derived phase occurs within the range $-\pi$ to π. It is, therefore, necessary to "unwrap" this effect so that the resulting phase is not constrained to this range. Once the interferogram has been unwrapped, the variation in phase follows topography if the deformation and noise component are negligible. It is then a case of scaling the image appropriately to map it into a Digital Elevation Model (DEM). This is done by a finding areas of low noise, and using these points to map to an existing DEM of the area, and applying a least squares regression over these tie points and using the resulting scale factor to multiply the phase image.

As a result of this interpolation, small changes in phase due to noise can introduce large discrepancies in the resulting DEM. These can be calculated using

$$\Delta h_{err} = \frac{\lambda R_1 \sin\theta}{4\pi B_\perp} \phi_{noise} \tag{6}$$

From our Radarsat scenes archive there are a theoretical 97 possible image forming pairs, from repeat orbits. Most of these pairs cannot, however, be used for interferometry because they have unacceptably low coherence. Figure 5.1 shows the distribution of particular levels of coherence within all those scenes. The bulk of pixels have a coherence level of 0.3, which is not sufficient. Figure 5.2 illustrates the effect of increasing coherence from 0.3 to 0.5.

Coherence images themselves can provide useful information in identifying sources of temporal change in a radar scene. However, it is important to be able to identify the source of decorrelation within the scene, Using the analysis of Zebker and Villasenor [1992], we can take:

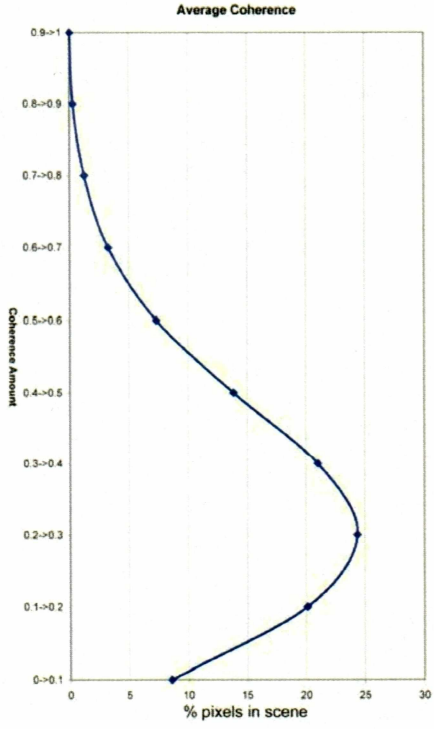

Figure 5.1, Average of coherence from the 97 suitable image pairs. Shows how an average coherence of between 0.2 and 0.3 dominates, too low to use for interferometry.

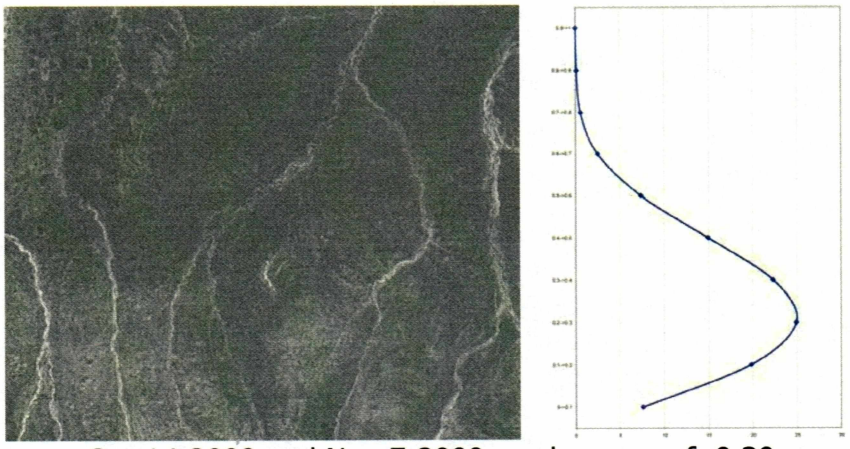

Oct-14-2000 and Nov-7-2000... coherence of 0.30

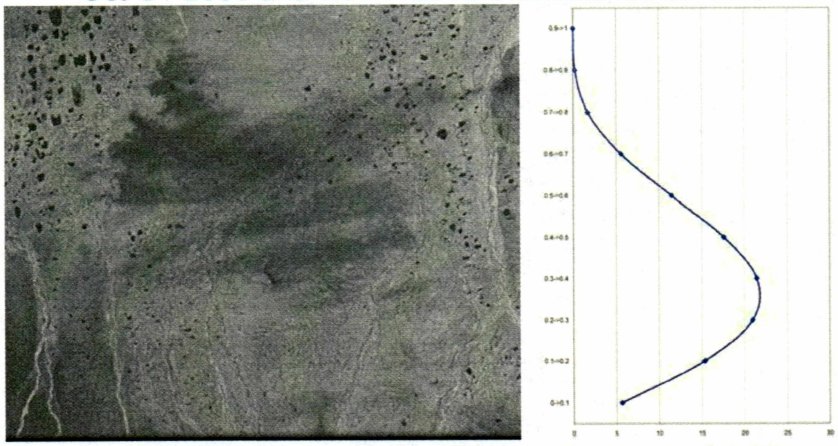

Aug-27-2000 and Sept-20-2000... coherence of 0.35

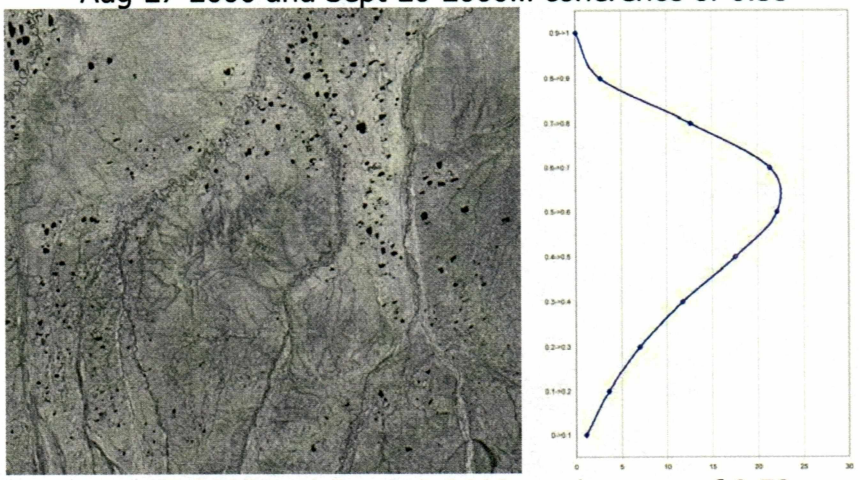

Aug-17-2000 and Sept-10-2000... coherence of 0.52

Figure 5.2, Example of low average coherence (top) of 0.3, a medium level of coherence (middle) 0.35 and excellent coherence (bottom) 0.52.

$$
\begin{aligned}
s_1 &= c + n_1 \\
s_2 &= c + n_2 \\
c &= \text{ Common signal} \\
n &= \text{ thermal noise at the sensor}
\end{aligned}
\tag{7}
$$

Since the signal and noise are not correlated, we can express this using the form of (1) as

$$
\begin{aligned}
\gamma_{\text{thermal}} &= \frac{|c|^2}{|c|^2 + |n|^2} \\
SNR &= \frac{|c|^2}{|n|^2} \\
\gamma_{thermal} &= \frac{1}{1 + SNR^{-1}}
\end{aligned}
\tag{8}
$$

if we expand (1) to include other sources of decorrelation, such as spatial and temporal components, we get

$$
\gamma_{total} = \gamma_{temporal} \cdot \gamma_{spatial} \cdot \gamma_{thermal} \tag{9}
$$

Expressing spatial decorrelation in a similar fashion as (7) and (8), we get

$$
\begin{aligned}
s_1 &= c + d_1 + n_1 \\
s_2 &= c + d_2 + n_2 \\
\gamma_{spatial} &= \frac{|c|^2}{|c|^2 + |d|^2} \\
\gamma_{spatial+thermal} &= \frac{|c|^2}{|c|^2 + |d|^2} \cdot \frac{1}{1 + SNR^{-1}}
\end{aligned}
\tag{10}
$$

Using our knowledge of the geometry of the satellite passes, and if we assume a surface of uniformly distributed uncorrelated scattering centres, an expression for γ_{spatial} resulting from parallel, not crossing orbits, can be derived.

$$
\begin{aligned}
\gamma_{spatial} &= 1 - \frac{2\cos\theta |\delta\theta| R_y}{\lambda} \\
\delta\theta &= \text{difference in look angle due to baseline separation} = \theta_1 - \theta_2 \\
R_y &= \text{Range Resolution}
\end{aligned}
\tag{11}
$$

this leads to a critical baseline, at which no scatterer can remain correlated as.

$$B_{critical} = \frac{\lambda r}{2R_y \cos^2 \theta} \qquad (12)$$

$$r = \text{slant range}$$

For the Radarsat standard mode, this gives a critical baseline of around 1000 m for beam 5, and 1900 m in beam mode 7. In practice a baseline exceeding 1/2 of these values will provide very low levels of coherence, due to antenna constraints and digital processing.

Examining the images in the archive, it is clear that in this arctic site, coherence is degraded on all baselines over 200 m (Figure 5.3). Radarsat differs from the ERS radar satellites by having a less stable orbit pattern. This manifests itself in a strong spread of delta perpendicular baselines. This also has an effect of degrading coherence as it induces a large difference in Doppler centroids between repeat images and a small rotation in the derived SAR scenes. Considering satellite passes with small perpendicular baselines, and perpendicular baseline far bellow the critical baseline, they still exhibit very low coherence. This in turn indicates how sensitive the coherence is to temporal change that occurs between repeat passes of at least 24 days. This also indicates that the temporal change signal is the dominant portion of the coherence degradation signal.

Figure 5.4 shows how coherence varies with time of year. It is clear from this chart that the propensity for low coherence is constant throughout the year and is not seasonally dependent. Lack of data in the first four months of the year, makes it tempting to infer that coherence is lower during this time. However, due to lack of images, this cannot be shown in this dataset.

Taking two sets of overlapping image pairs from 2000, the distribution of coherence within the scene can be analysed. Figure 5.5 shows that there is a strong pattern of higher coherence with lower elevation (R^2 value of 0.73 and

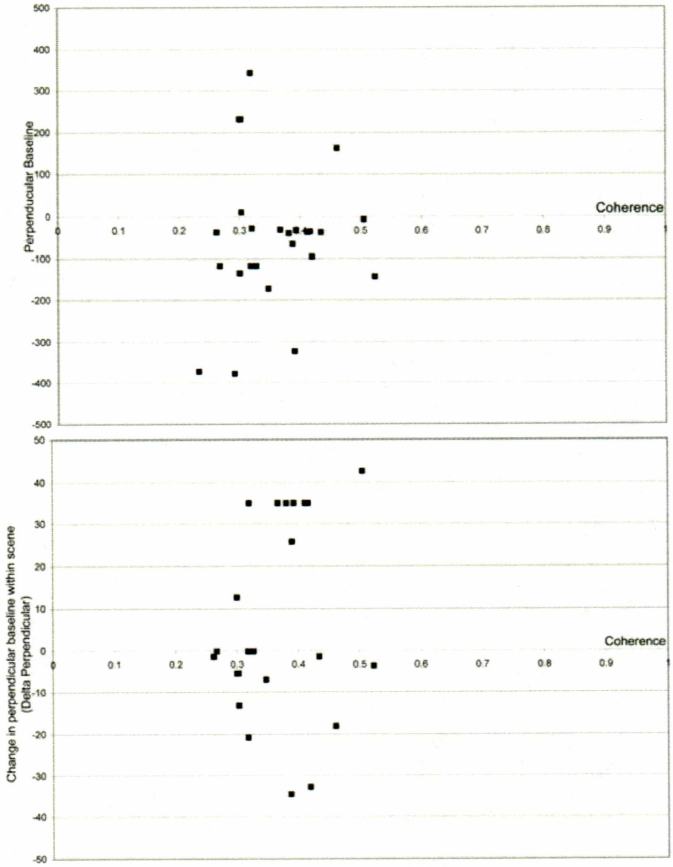

Figure 5.3, Relationship between perpendicular and delta perpendicular baseline to scene coherence. No images with a perpendicular baseline exceeding 500m achieved a coherence greater than 0.2 and so are not shown.

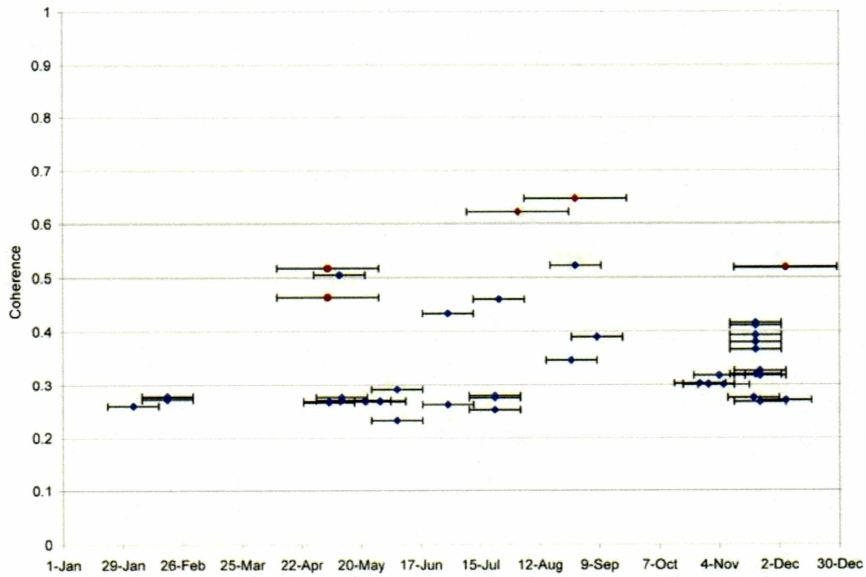

Figure 5.4, Coherence expressed as a function of time of year. Brown markers indicate scenes create from satellite passes 48 days apart, and their coherence is adjust to allow them to be compared with 24 day repeat passes.

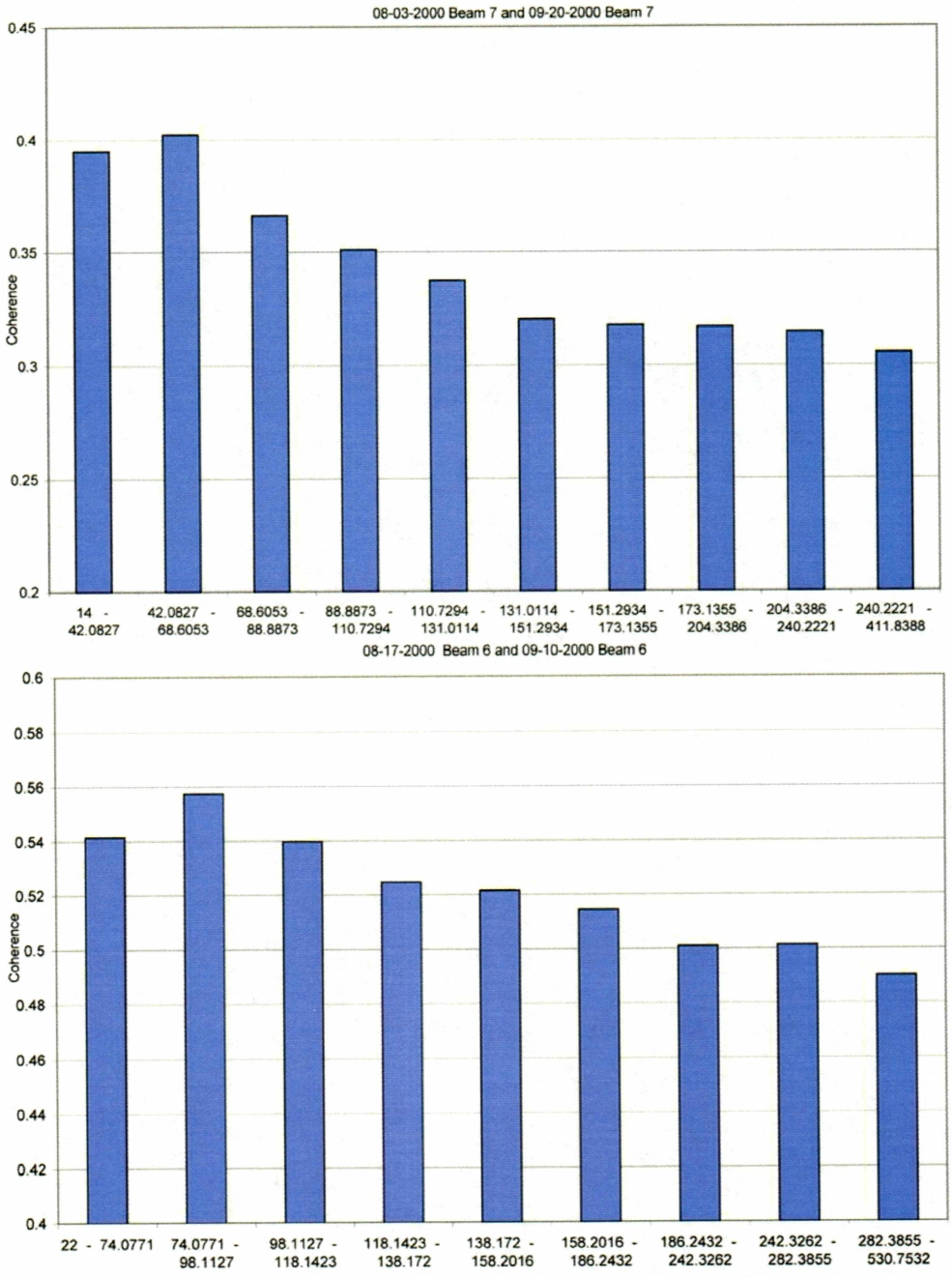

Figure 5.5, Comparison between mean coherence for different altitudes within each scene. Lower areas have a significantly higher coherence than higher regions. Elevation bins are determined by 10% total scene occurrence.

0.78 respectively). In this Figure the DEM of a scene was analysed and reduced into 10 elevation groups of equal pixel occurrence within the scene. The slight difference in geographic area between Figures 5.5a and 5.5b is the reason that the elevation bins are slightly different between the beam mode 7 and the beam mode 6 data.

From Figure 5.5, we can see, in addition to the obvious trend, a fall of coherence in the highest elevation bin; this is due to the increase in steep slopes in this bin. The fall of coherence in the lowest elevation bin is due to the fact that the majority of lakes occur in this area. Their significant surface area is too dynamic to maintain coherence between scenes, due to the open water and wave effects in summer and ice growth at other times of year.

The NDVI is used to assist in the analysis of INSAR coherence. NDVI, of the Sagwon area, correlates highly with elevation and has a R^2 value of 0.85. This can be easily seen in Figure 5.6, which also indicates the NDVI values of MNT and MAT regions within the area and their corresponding standard deviations, illustrated with the green and red shaded regions. The NDVI image was generated from a MODIS 250 m resolution scene of 17th July 2002.

Comparing the NDVI directly to coherence shows an interesting pattern. There is a strong correlation between NDVI and coherence for the NDVI range between 0.6 and 0.69, with an R^2 of 0.92. For NDVI greater than 0.69, NDVI and coherence has no strong correlation, indicating a critical threshold of leaf index above which coherence remains low (Figure 5.7). The fall of coherence in low NDVI is due to the significant lake presence within this data bin.

The strong correlation of NDVI to coherence is expected as leafs would have a strong scattering effect, and fresh growth causes additional random interferometric phase variations in a pixel neighbourhood. Therefore, the increase of their occurrence would degrade the coherence more. If the relationship between NDVI and coherence held strictly for all NDVI, then the

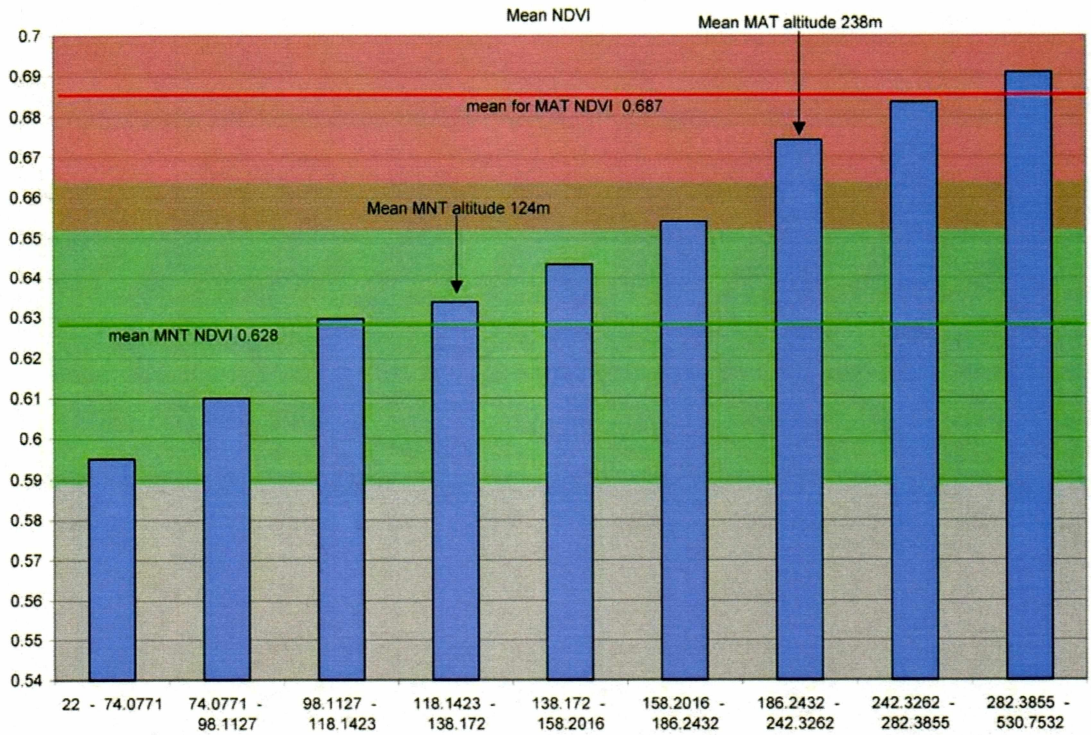

Figure 5.6, Correlation of NDVI to elevation, showing the mean NDVI of MNT (green) and MAT (red), and indicating their standard deviations. Elevation is grouped into bins of 10% of total scene occurrence. NDVI is derived from a MODIS image of July 17th 2002.

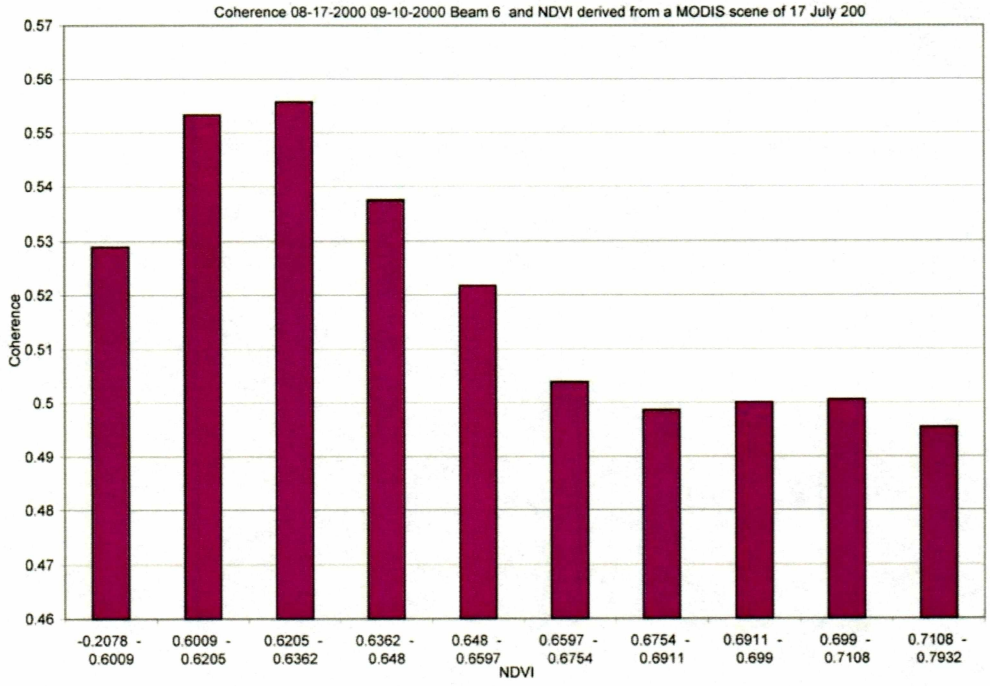

Figure 5.7, Association of NDVI and Coherence, lower NDVI has a significantly higher coherence, very low NDVI the result of pixels of open water including lake surfaces, causes lower coherence due to the very dynamic nature of these surfaces.

boundary between MAT and MNT would be clear within the coherence images. But the relationship breaks down above 0.66, which by coincidence is exactly the region where the standard deviations of MNT and MAT overlap, (see the white areas in Figure 5.6). Consequently, in the overlapped region the MAT / MNT boundary is not seen clearly as there is very little difference in coherence here. In contrast, however, areas that are strongly MNT dominated show up clearly as having higher coherence. A coherence image showing this effect is shown in Figure 5.8. The areas of purple correspond well to the areas of ambiguity with similar MAT/MNT NDVI values. These areas appear as areas of white tone in the subsequent Figure 5.9 that shows the NDVI image thresholded and artificially coloured to show the three regions, (MNT blue, MAT yellow, MNT not detectable in coherence images White).

With the exception of the areas noted, all the coherence images with high enough coherence for features to be seen, (an average coherence above 0.35) show the same regions of MNT and MAT tundra see (Figure 5.10) which has a coherence of 0.52.

Areas of high enough coherence, to allow for a phase image to be established, can be used to infer topography; however, a small error in phase can lead to large error in height, as shown in equation 6. To quantify how coherence effects the accuracy of the derived DEM, the interferometric pair of August 17th 2000 and September 10th 2000, with a baseline of –146 m, was co-registered to an existing coarser resolution DEM. Elevation varies within this geographic area from 22 m up to 500 m, any pixel taken within the SAR DEM image could have an error of up to 530 m (the maximum error seen in this DEM). The mean error across an area is substantially smaller Figure 5.11 shows the DEMs concerned and the distribution of the error within the scene. A break down of the error with coherence is shown in Figure 5.12, indicating that though coherence does have a distinct effect, it is of a small magnitude, when compared

Figure 5.8, Coherence image showing that some regions, shown in purple are misidentified as being with the MAT region (to the South). Examining the MODIS NDVI image shows these areas have a value that is not well differentiated by coherence.
Coherence between 08-03-2000 and 08-27-2000 beam mode 7.

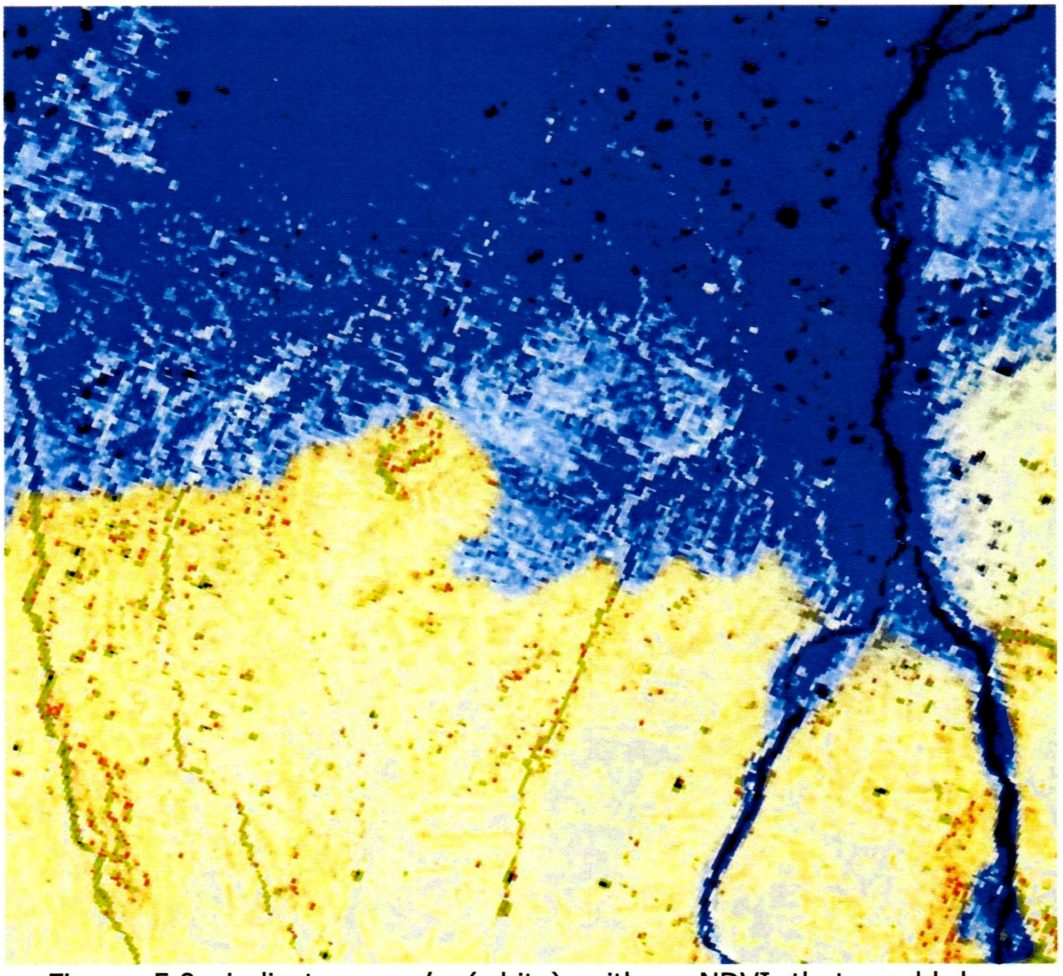

Figure 5.9, indicates area's (white) with a NDVI that could be interpreted as the wrong tundra type in coherence images, yellow represents MAT and blue MNT, intermediate NDVI known to be MNT are shown in white.

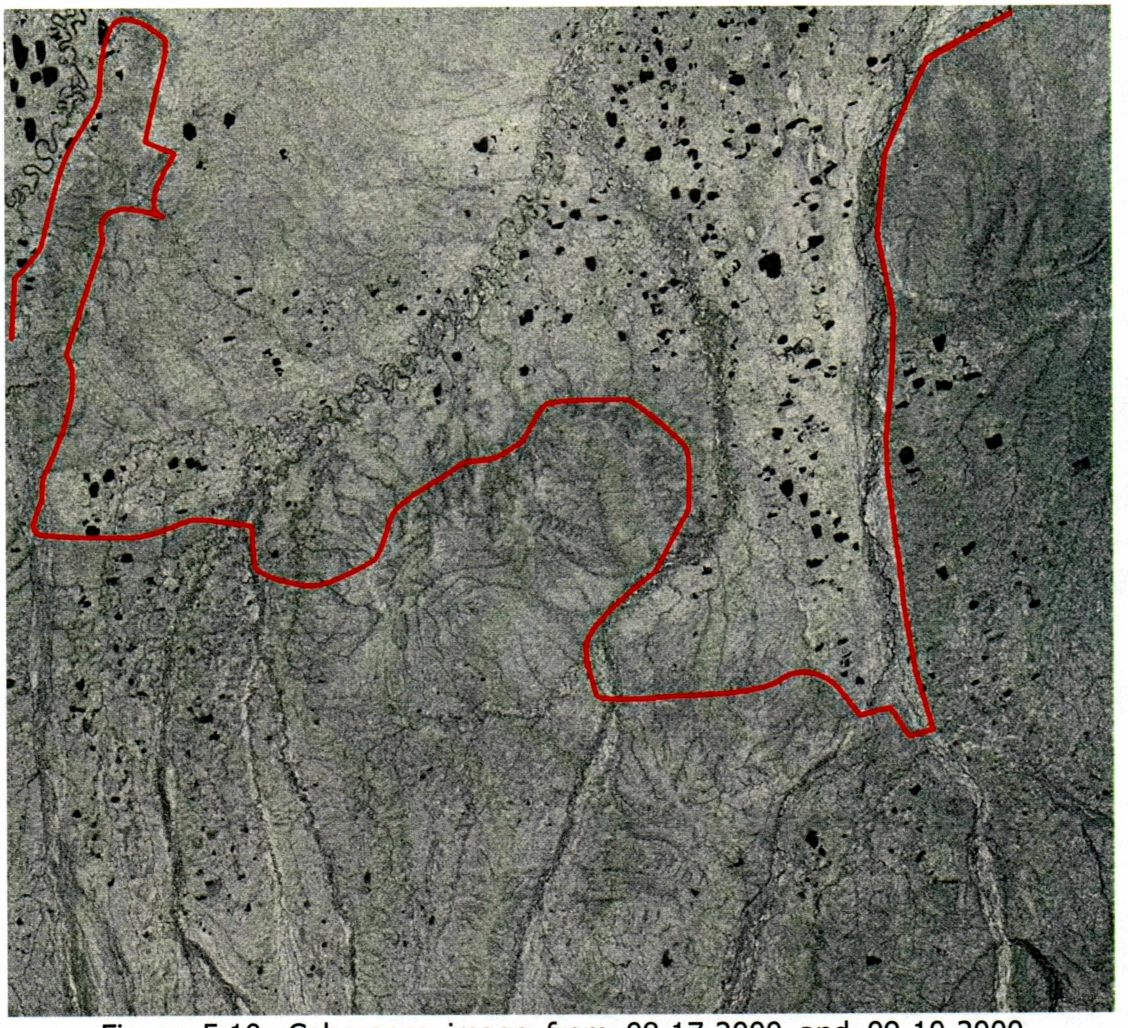

Figure 5.10, Coherence image from 08-17-2000 and 09-10-2000 beam mode 6, the boundary is between MNT and MAT is highlighted, MAT to the South (bottom).

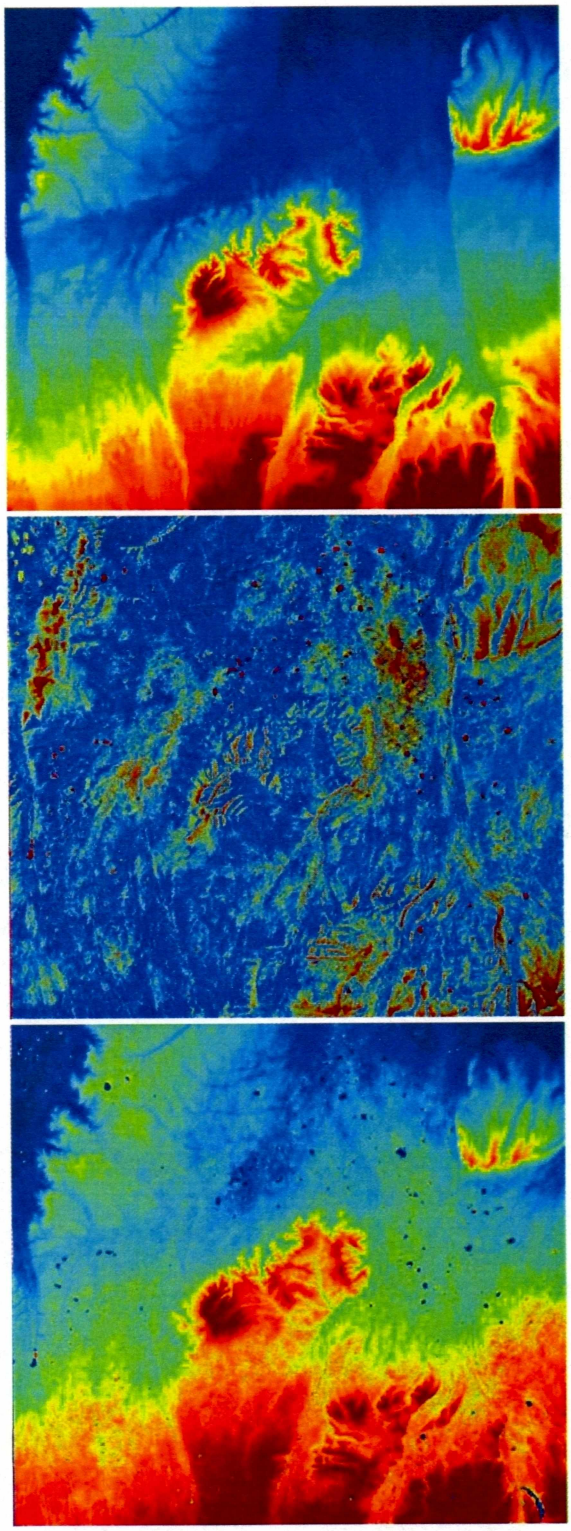

Figure 5.11, the Reference DEM, difference between that and the INSAR DEM and the INSAR derived DEM.

The difference in height is normally fairly small hence dark blue colour predominates in the difference image, however, some areas have a substantial difference.

Scene's are approximately 100km wide, and the colour scale is persistent across images, and indicates 500m of topography, Blue low elevation, Red high elevation.

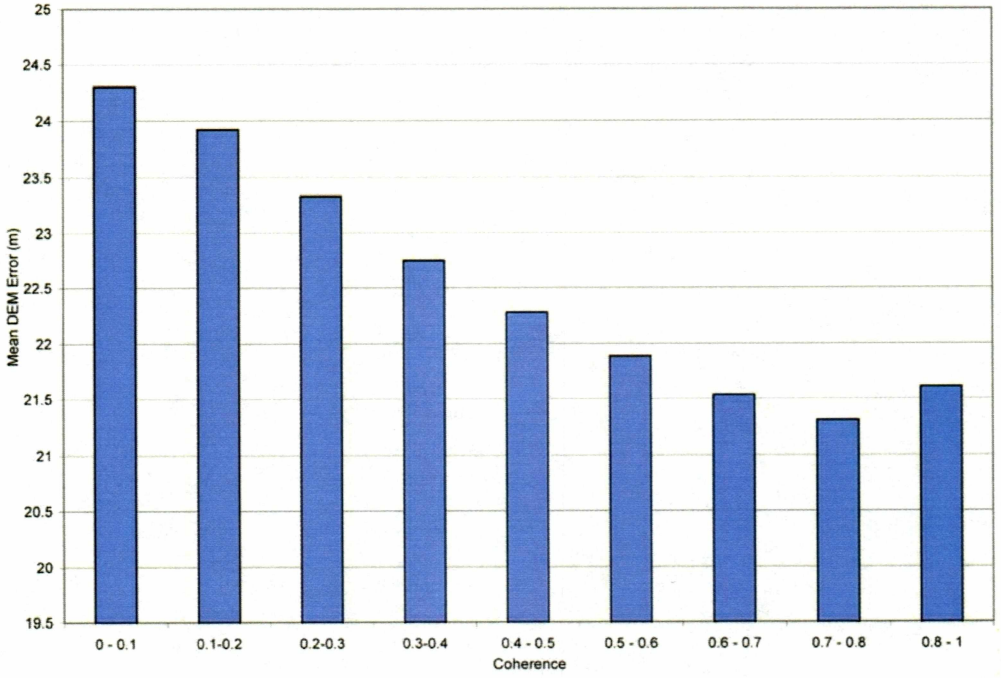

Figure 5.12, mean height error in a DEM derived from an INSAR pair, 08-17-2000 and 09-10-2000 beam 6, indicating a minimum error for higher coherence values, and showing that coherence above 0.8 is anomalous and due to slope effects rather than actual noise within the phase.

to the full range of error possible. Areas of strong slope can give anomalously high coherence values; due to this and their higher noise component the bin of coherence from 0.8 to 1, shows a small increase in mean error.

To illustrate the nature of this height error, Figure 5.13, shows this broken down by coherence and normalised to the number of pixels within each coherence bin. The amount of overall error in the derived DEMs makes comparison between DEM difficult; to overcome these issues, we performed a careful analysis of interferometric phase components.

The radar phase surface of a single image can be described using

$$\phi = \frac{-4\pi R}{\lambda} \tag{13}$$

Then if we introduce some deformation to the phase through δR then we can rewrite (13) as

$$\phi = \frac{-4\pi (R + \delta R)}{\lambda} \tag{14}$$

Using another radar image or the same area and subtracting from (14) gives

$$\phi = \frac{-4\pi (R_1 + \delta R_1 - R_2)}{\lambda}$$

$$\phi = \underbrace{\frac{-4\pi (R_1 - R_2)}{\lambda}}_{\text{the terrain Component}} - \underbrace{\frac{4\pi (\delta R_1)}{\lambda}}_{\text{the deformation component}} \tag{15}$$

$$\nabla\phi = \frac{-4\pi\delta R_1}{\lambda}$$

Substituting $\Delta\Phi$ for Φ_{noise} in equation 6, we can deduce that phase distortions due to deformation and other errors would produce strong height errors, if they are not removed during DEM generation. If terrain effects and deformation components can be separated the resulting phase image revels only the deformation that has occurred in the period.

Typically DEMS are generated using ERS interferometry, where the 1 day apart tandem mission allowed the production of high quality interferograms, with

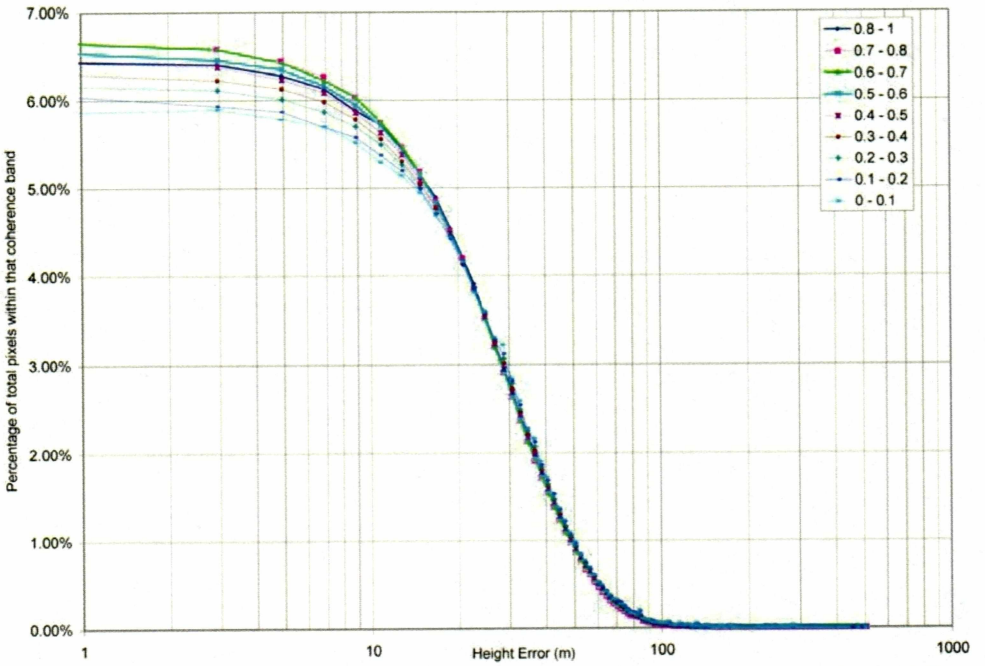

Figure 5.13, Shows how the error in height of pixels is distributed for different levels of coherence. Percentage pixels, refers to the number of pixels within that coherence bin, rather than pixels of the scene.

little noise component and deformation involved. A pair of other ERS images, with a greater temporal separation, when combined with ERS tandem is likely to produce a pattern of the deformation in this long period.

Using Radarsat interferograms the results are slightly more ambiguous, the 24 day repeat orbit means that any two pairs of images are likely to include surface deformation in them. Therefore, separating terrain and deformation effects requires further knowledge or assumptions.

Despite this limitation we attempted to apply the Dinsar technique to Radarsat data. Practice, however, has proved trickier. From our knowledge of when deformation is likely to occur in scenes either prior to the freezing of the active layer, or after the active layer has frozen and water migration and lensing is causing it to heave. Images acquired during July and August should show the ground to have fully relaxed and the active layer completely unfrozen. Images from October through to May should show some signs of deformation [Li and Wang 1999].

Of the 50 scenes of the area, the majority of interferogram pairs do not produce high enough coherence to form decent interferograms. Those pairs that have a small baseline are likely to form better interferograms. However, the sensitivity of those pairs to topography is degraded. From those scenes one can produce a DEM, but the elevation errors tend to be large. Finding another pair that spans the deformation is even harder.

The principle of INSAR techniques requires that all the interferogram pairs need to be from the same beam mode, further constraining our analysis. With all of the constraints, only three interferogram pairs have been found suitable in our change analysis.

From beam mode 5, two image pairs are suitable: one dated April 28th 2001, and May 22nd 2001, with a perpendicular baseline of –24 m and a coherence of 0.51 and the other from 9th July 2001 and August 26th 2001 with a

perpendicular baseline of –58 m and a coherence of 0.39. This combination of images is not ideal due to the 48 day repeat in the second scene and the issue of having to use the scene with deformation as the topography scene. Both these scenes have very small perpendicular baselines, making them relatively insensitive to topographic change. The image is of an area just to the south of Sagwon, and only shows MAT. The processed differential interferogram is shown in Figure 5.14. The image is not easy to interpret; the regions of similar differential phase do not correlate with any lithographic group, and the strong arch look pattern in the upper portion of the image suggests that some other effect may be dominating the signal. Probably the pattern seen is due to the effect of a differing thickness of snow layer, though we have no evidence to support this hypothesis.

The deformation scene from July and August is also likely to exhibit the effects of differing moisture content in the ground. From another set of images from beam 7, the large value of the delta perpendicular component causes some difficulty in the generation of a change pattern. Consequently, the resultant differential interferogram shown in Figure 5.15 has a strong obscuring fringe pattern.

A single set of scenes are suitable, from the slightly further north Sagwon area. However, they suffer from the effects of low coherence. The Dinsar image is shown in Figure 5.16. The deformation shown in this image is difficult to interpret, and is well within a fringe, indicating that much less than 2.56 cm of displacement has taken place.

The use of Radarsat for Differential interferometry is limited by a number of factors: principally, the 24 day repeat orbit, the lack of high quality repeat orbits, the high sensitivity of coherence to ground changes and the lack of a database for cross-referencing satellite orbits to establish the baseline of image pairs prior to ordering. However, despite these limiting factors, the results

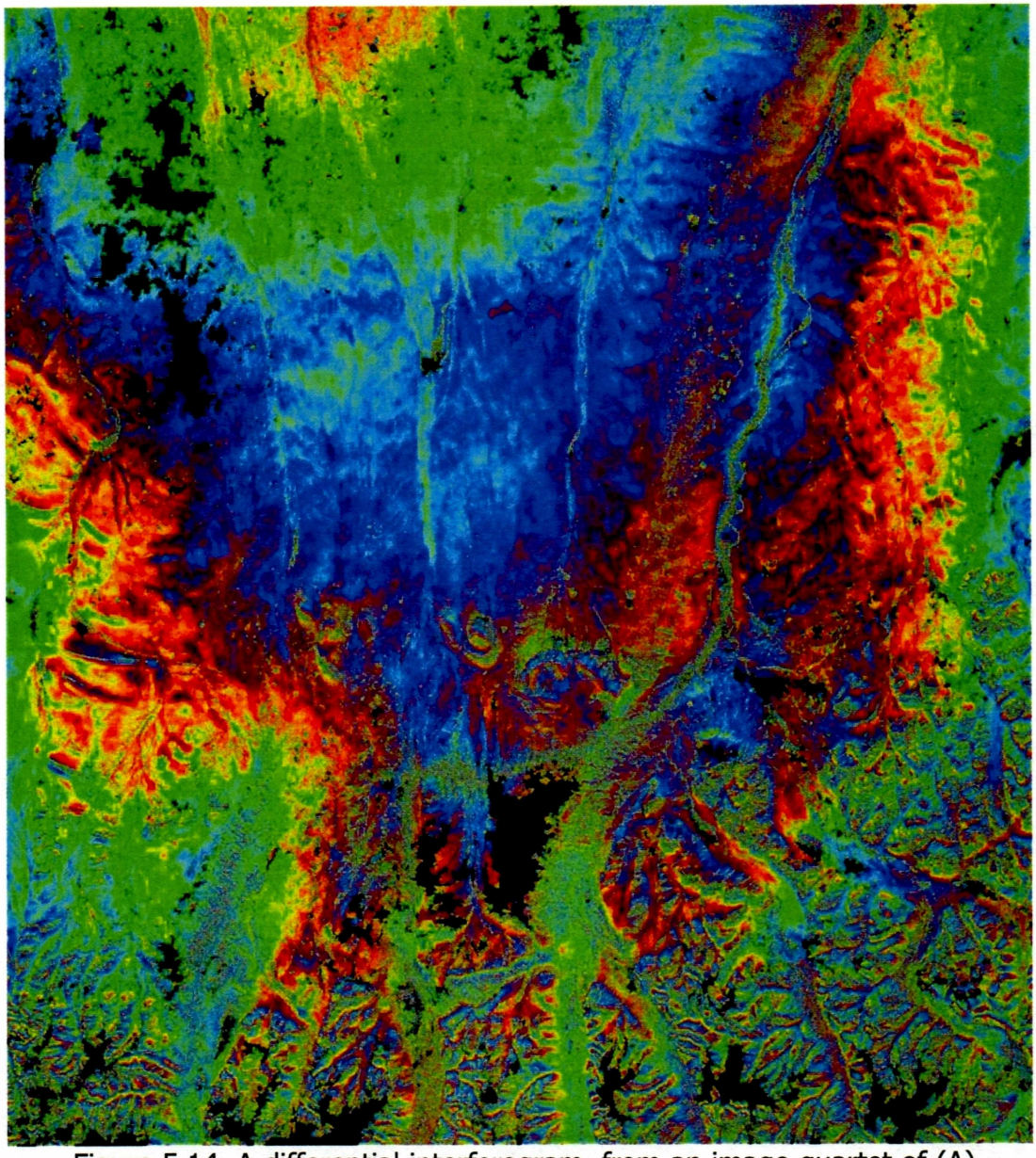

Figure 5.14, A differential interferogram, from an image quartet of (A) April 28th and May 22nd 2001, and (B) July 9th and August 26th 2001. the image is centred to the south of Sagwon. The deformation pattern is not easily interpreted, and is most likely reflective of the distribution of snow with the area.

Base lines for the images are:	$\perp$ (perpendicular),	$\Delta\perp$	$\parallel$ (parallel),	$\Delta\parallel$
Topography scene (A)	–23.81m	14.62m	-60.37m	-10.39m
Deformation scene (B)	–58.44m	-12.38m	104.69m	7.9m

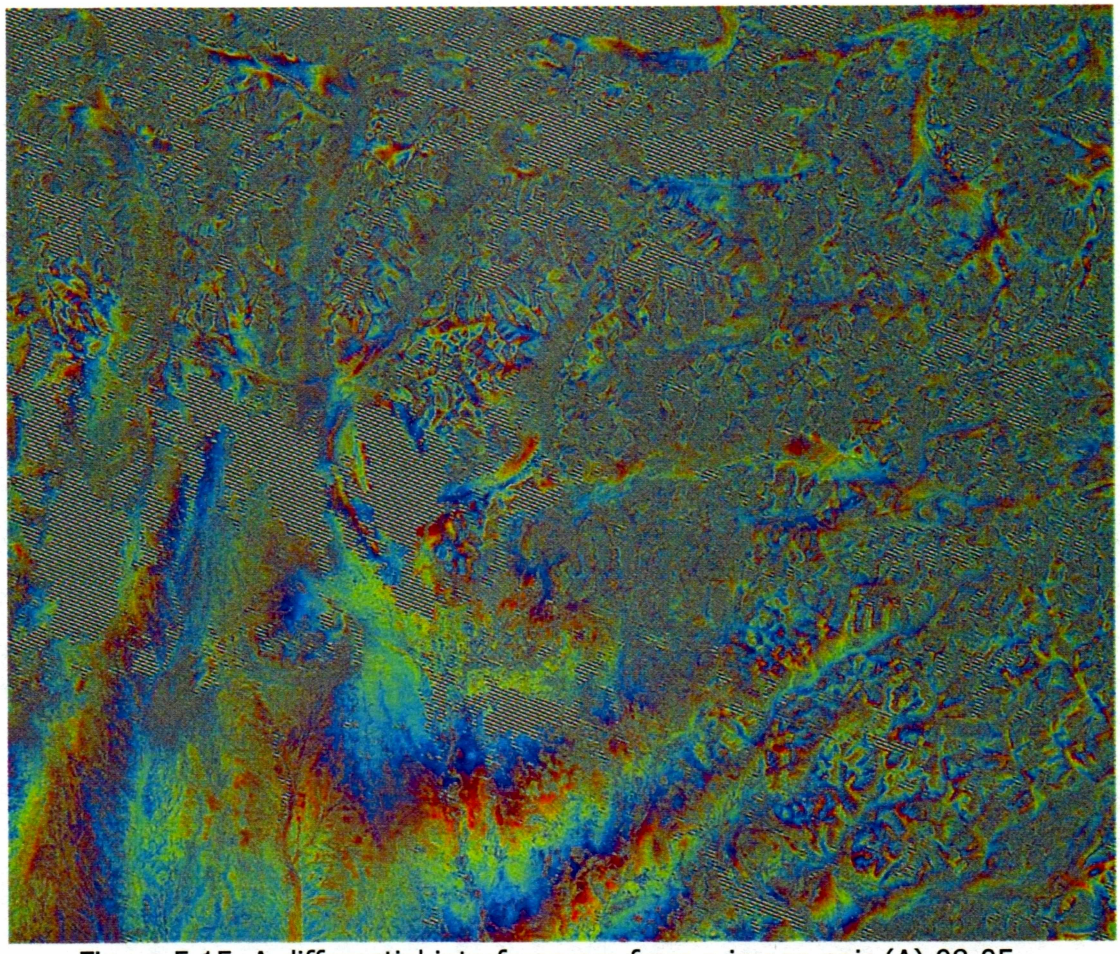

Figure 5.15, A differential interferogram from a image pair (A) 08-05-2001 / 09-22-2001 and a image pair (B) 11-09-2001 / 12-03-2001. both images have a strong delta perpendicular baseline component which introduces the orbital fringes seen.

Base lines for the images are:	$\perp$ (perpendicular),	$\Delta\perp$	$\parallel$ (parallel),	$\Delta\parallel$
Topography scene (A):	-95.50	-32.66	159.02	26.52
Deformation scene (B):	-39.42	35.10	-13.23	-30.36

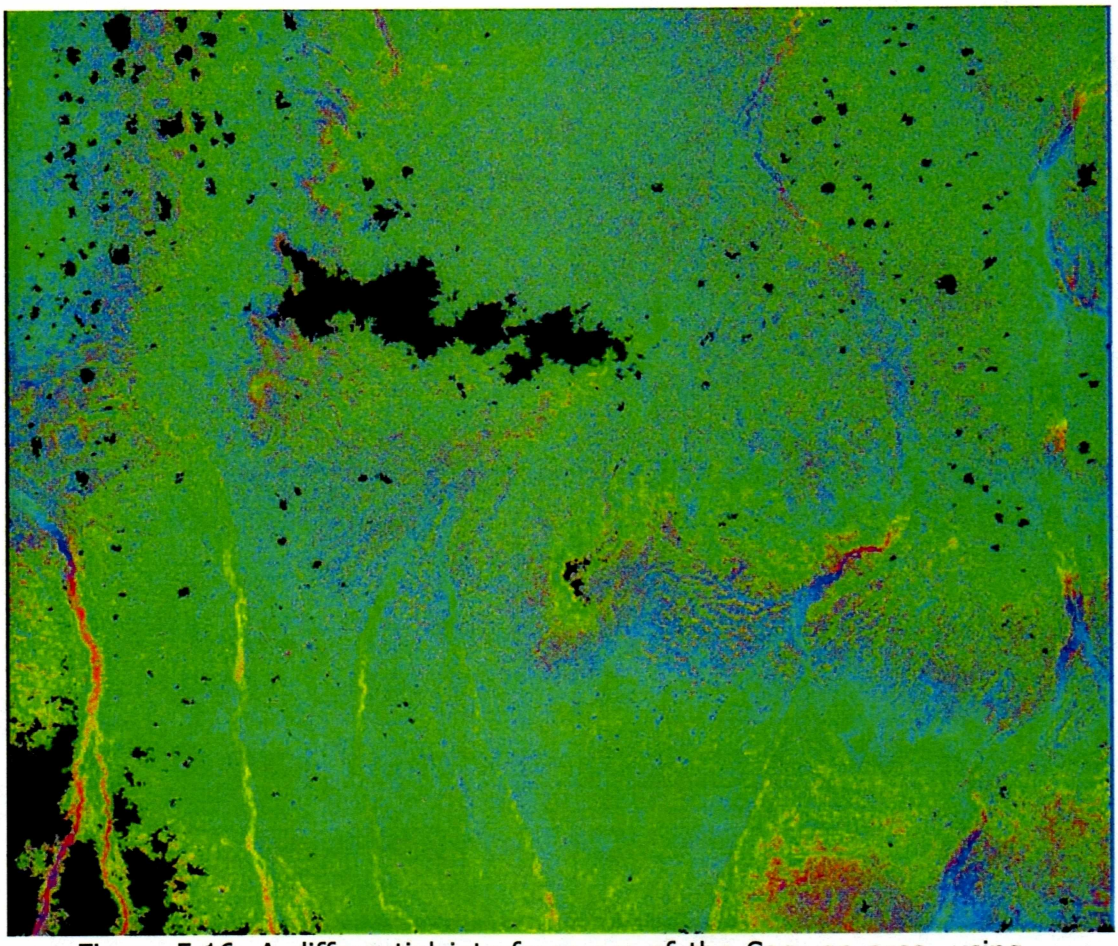

Figure 5.16, A differential interferogram of the Sagwon area, using images from Aug 27th 2000 and Sept 20th 2000 for topography (A), and Oct 14th 2000 and Nov 7th 2000 for deformation. The image suffers from residual orbital fringes due to the delta perpendicular component.

Baselines	: ⊥ (perpendicular),	Δ⊥	∥ (parallel),	Δ∥
Topographic (A)	: -328.20	5.15	298.45	-5.06
Deformation (B)	: 13.29	-5.69	10.38	3.24

obtained above show that Radarsat does have potential and can be used for differential interferometry.

Discussion

The use of radar imagery holds certain advantages over that of optical technology, principally its ability to "see" through clouds and the fine ground resolution of its images. However, there are many caveats involved with the interpretation of images derived from radar products, especially when the brain tries to convey an optical interpretation on to the scene.

Within the Arctic tundra environment radar scenes hold strong advantages over optical imagery, in that some snow cover penetration is possible, broad inferences of the nature of snow cover can be established, and the effects due to the freezing the ground surface can be investigated. Like all satellite based observations there are issues relating to the time between image acquisition periods. Radarsat has a temporal repeat orbit of 24 days that make its facilitation in isolating dates of freeze-up and thaw less than ideal. However, through harnessing several beam modes, it is possible to reduce the period between visits. This, however, will depend on the location of the study region but is especially feasible at high latitudes.

Using information from backscatter images, it is possible to observe features not readily visible in the optical spectrum. Developed in this thesis is a technique that uses empirical orthogonal functions to enhance the visibility of a boundary between acidic and non-acidic tundra utilizing the difference in soil texture and vegetation coverage to differentiate the regions. The disadvantage of this technique is that it requires a number of radar scenes to accurately express the boundary. It is only through the use of this statistical technique that a strong boundary can be seen, and as such it shows the worth of what would otherwise be questionable and inconsistent dataset.

Coherence images, taken from repeat pass orbits, contain information that is distinct from what can be obtained from the amplitude images. The coherence images are very sensitive to surface change, and it is rare for coherence to be

maintained beyond 24 days. This sensitivity can have strong advantages in scenes with high coherence clearly delineating small rivers and other surface features that would otherwise be hard to see in the amplitude images alone.

The generally low coherence between scenes has a strong adverse effect on the processing of interferometric pairs, though coherence, above a base level allowing formation of an unwrapped interferogram, does not strongly effect the accuracy of derived DEMs. When compared to coherent phase noise, it does have a strong threshold effect. Image pairs with a coherence of less the 0.4 have difficulty in being fully unwrapped which in turn limits their use in differential interferometry.

Using differential interferometry to derive surface deformation is very difficult in the Arctic region using Radarsat datasets. The frequently large delta perpendicular baselines, introduces additional difficulty in removing residual orbital fringes. The nature of the tundra surface is also not conducive to successful DINSAR work, as the presence of snow and the change of snow cover between scenes decorrelate SAR images in the INSAR pairs and significantly obscure any ground surface deformation signal during the thaw and freeze periods.

Further work with variations on the DINSAR technique that allow the mixing of beam modes or the productive use of scenes with a large delta perpendicular baseline, would likely increase both the quantity and quality of derived DINSAR results. The experience of attempting to use the DINSAR technique with Radarsat data and in this challenging environment underlies the sensitivities of this method that are both its strength and weakness.

Conclusion

This thesis presents the results of an analysis of two years of Radarsat standard beam mode images of an area centred on Sagwon in Alaska. Three principle types of data were used for the analysis, the calibrated amplitude images, coherence images between two repeat orbit satellite passes, and differential interferometric SAR.

The backscatter images show strongly the seasonal progression, with a strong difference in backscatter between frozen and unfrozen ground. Further analysis of these images using Empirical Orthogonal Functions has shown that it is possible to use these images to show the regions of Moist Acidic Tundra and Moist Non-acidic Tundra. The technique leverages the slight change in backscatter due to a change sand to clay ratio, consistent with that boundary to produce a resultant image with a substantially clearer MNT/MAT boundary.

Coherence levels are strongly correlated to NDVI values bellow a critical level of 0.69; above this boundary there is no significant correlation with NDVI. This factor makes the boundary between tundra types visible in the coherence images; however, as the top few percent of MNT regions have a NDVI above this 0.69 value, they become confused with the regions of MAT. This makes the use of coherence images in tundra type delineation somewhat limited. The coherence images, however, are very sensitive to surface change, and as a result show drainage channels and water pathways within the arctic tundra distinctly, even in images with snow cover above them.

The use of DINSAR images to estimate the amount of surface heave of the active layer has been explored. However, limitations on the quality of repeat pass data, due to both environmental factors and factors relating to the operation Radarsat satellite, have meant that the results obtained are both of poor quality and are difficult to interpret. The DINSAR results have shown the

strong sensitivity of the method, and in turn a further refinement of processing technique and perhaps a little luck, would allow Radarsat to be used for DINSAR work in the Arctic tundra environment.

In conclusion, this study has shown that radar images of the Arctic tundra can yield extensive further information about the surface properties of the tundra and their temporal change. The ability of radar to disregard cloud cover and also provide some degree of snow penetration, make the use of the radar scene's attractive to anyone involved in Arctic tundra research.

References.

Bockheim J, Walker D, Everett L, Nelson F, Shiklomanov N, 1998, Soils and Cryoturbation in Moist Nonacidic and Acidic Tundra in the Kuparuk River basin, Arctic Alaska, USA. Arctic and Alpine Research, Vol 30, No 2, 166-174.

Brisco B, Brown R, 1998, Agricultural Applications with Radar, in Principles and Applications of Imaging Radar, Manual of Remote Sensing, Volume 2,3rd Edition. Ed. F Henderson, A Lewis and R Ryerson, Wiley New-York , 131-181.

Eslinger D, O'Brien J, Iverson R, 1989, Emprical Orthogonal Function Analysis of Cloud-Containing Coastal Zone Color Scanner Images of Northeastern North American Coastal Waters, Journal of Geophysical Research, Vol 94, No. C8, 10884-10890.

Everson R, Cornillon P, Sirovich L, Webber A, 1995, An Empirical Eigenfunction Analysis of Sea Surface Temperatures in the Western North Atlantic, Journal of Physical Oceanography, Vol 27, No. 3, 468-479.

Hallikainen M, Ulaby F, Dobson M, El-Rayes M, Wu L, 1985, Microwave Dielectric Behavior of wet soil – part 1 : Empirical Models and Experimental Observations, IEEE Transactions on Geoscience and Remote Sensing, Vol GE-23 No 1, 25-34.

Hinzman L, Goering D, Kane D, 1998, a distributed thermal model for calculating soil temperature profiles and depth of thaw in permafrost regions, Journal of Geophysical Research, Vol 103 No D22, 28975-28991.

Jeffries, M. O., Morris K, Weeks W. F., Wakabayashi H, 1994, Structural-stratigraphic features and ERS-1 SAR backscatter characteristics of ice growing on shallow lakes in N.W. Alaska, winter 1991-92, Journal of Geophysical Research, 99(C11), 22459-22471.

Koskinen J., Pulliainen J., Hallikainen M., 2000, Effect of Snow Wetness to C-Band Backscatter - A Modeling Approach, Report 41, Laboratory of Space Technology, Helsinki University of Technology, Espoo, 20.

Lewis A , Henderson F, 1998, Radar Fundamentals: the Geoscience Perspective, in Principles and Applications of Imaging Radar, Manual of Remote Sensing, Volume 2,3rd Edition. Ed. F Henderson, A Lewis and R Ryerson, Wiley New-York, 131-181.

Lewkowicz A, Duguay C, 1999, Detection of permafrost features using SPOT panchromatic imagery, Fosheim Peninsula, Ellesmere Island NWT, Canadian Journal of Remote Sensing, Vol 25, No 1, 34-44.

Li S, Wang Z, 1999, Detection of winter frost heaving of the active layer of arctic permafrost using SAR differential interferograms, IEEE Transactions of Geoscience and Remote Sensing, 1946 – 1948.

McFadden J, Liston G, Sturm M, Pielke S, Chapin S, 2001, Interactions of shrubs and snow in arctic tundra: measurements and models, Soil. Vegetation. Atmosphere Transfer Schemes and Large-Scale Hydrological Models (Proceedings of a symposium held during the Sixth IAHS Scientific Assembly at Maastricht, The Netherlands, July 2001). IAHS Publ. no. 270.

McMichael C, Hope A, Stow D, Fleming J, 1997, The relation between active layer depth and a spectral vegetation index in artic tundra landscapes of the north slope of Alaska, Int. J. Remote Sensing, Vol 18, No 11, 2371-2382.

Mironov V, Komarov S, 2000, Microwave remote sensing of Soils. Novosibirsk: Publishing house of the Siberian branch of the Russian Academy of Sciences, in Russian.

Muller S, Racoviteanu A, Walker D, 1999, Landsat MSS-derived land cover map of northern Alaska: extrapolation methods and a comparison with photo-interpreted and AVHRR derived maps, INT. J. Remote Sensing, Vol 20, No 15 & 16, 2921 – 2946.

Peddle D, Franklin S, 1993, Classification of Permafrost active layer depth from remotely sensed and topographic evidence, Remote Sensing of the Environment, Elsevier Science Publishing, New York, No 44, 67-80.

Raney R, 1998, in Principles and Applications of Imaging Radar, Manual of Remote Sensing, Volume 2,3rd Edition, Ed. F Henderson, A Lewis and R Robertson, Wiley New-York , 9-130.

Rignot E, Way J, 1994, Monitoring Freeze-Thaw Cycles along North-South Alaskan Transects Using ERS-1 SAR, Remote Sensing of the Environment, Vol 49, 131-137.

Ulaby F, Dobson M, 1998,Mapping soil moisture distribution with imaging radar, in Principles and Applications of Imaging Radar, Manual of Remote Sensing,

Volume 2,3rd Edition. Ed. F Henderson, A Lewis and R Ryerson, Wiley New-York, 407 – 433.

Walker D, Auerbach N, Bockheim J, Chapin F, Euguster W, King J, McFadden J, Michaelson G, Nelson F, Oechel W, Ping C, Reeburg W, Regli S, Shiklomanov N, Vourlitis G, 1998, Energy and trace gas fluxes across a soil pH boundary in the Arctic, Nature, 394, 469-472.

Wegmuller U, Matzler C, Schanda E, 1989, Microwave signatures of bare soils, Advanced Space Research, Vol 9, 307- 316.

Zebker H, Goldstein R, 1986, Topographic mapping from interferometric SAR observations, Journal of Geophysical Research, Vol. 91, No B5, 4993-4999.

Zebker H, Villasenor J, 1992, Decorrelation in interfrometric Radar Echoes, IEEE transactions on Geoscience and Remote Sensing, Vol 30, No 5, 950-959.

Zebker H, Werner G, Rosen P, Hensley S, 1994, Accuracy of topographic Maps derived from ERS-1 interferometric Radar, IEEE transaction on Geoscience and remote sensing, Vol 32, No 4.

Appendix 1,
Source Scenes

Table A.1, Date Occurrence of the Radarsat Scenes

Radarsat Beam mode 5	Radarsat Beam mode 6	Radarsat Beam mode 7
28-Jan-00	2-Mar-00	29-Apr-00
23-Apr-00	9-Mar-00	22-May-00
9-May-00	17-Aug-00	10-Jul-00
16-May-00	10-Sep-00	3-Aug-00
26-May-00	4-Oct-00	27-Aug-00
3-Jun-00	28-Oct-00	20-Sep-00
10-Jun-00	1-Jun-01	14-Oct-00
20-Jun-00	5-Sep-01	7-Nov-00
18-Oct-00	29-Sep-01	14-Nov-00
25-Oct-00	23-Oct-01	25-May-01
11-Nov-00	16-Nov-01	18-Jun-01
18-Nov-00		12-Jul-01
25-Nov-00		5-Aug-01
5-Dec-00		22-Sep-01
29-Dec-00		9-Nov-01
22-Jan-01		3-Dec-01
15-Feb-01		
18-Apr-01		
28-Apr-01		
22-May-01		
9-Jul-01		

Appendix 2,

Table A.2, Radarsat Standard Beam details

RADARSAT Modes:	Near Range Incidence Angle	Far Range Incidence Angle	Near Range Resolution (m)	Far Range Resolution (m)	Near Ground Range (km)	Far Ground Range (km)	Swath Width (km)
ST5	36.54	42.23	23.21	20.56	519.00	627.32	108.32
ST6	41.46	46.58	20.87	19.02	611.88	720.21	108.33
ST7	44.87	49.42	19.58	18.19	682.45	786.86	104.41

Source ASF website

http://www.asf.alaska.edu/radarsat/radarsat_beam_ground_params.html

checked as of 8th April 2002.